iScience

CellPress
OPEN ACCESS

Article

Fallopian tube single cell analysis reveals myeloid cell alterations in high-grade serous ovarian cancer

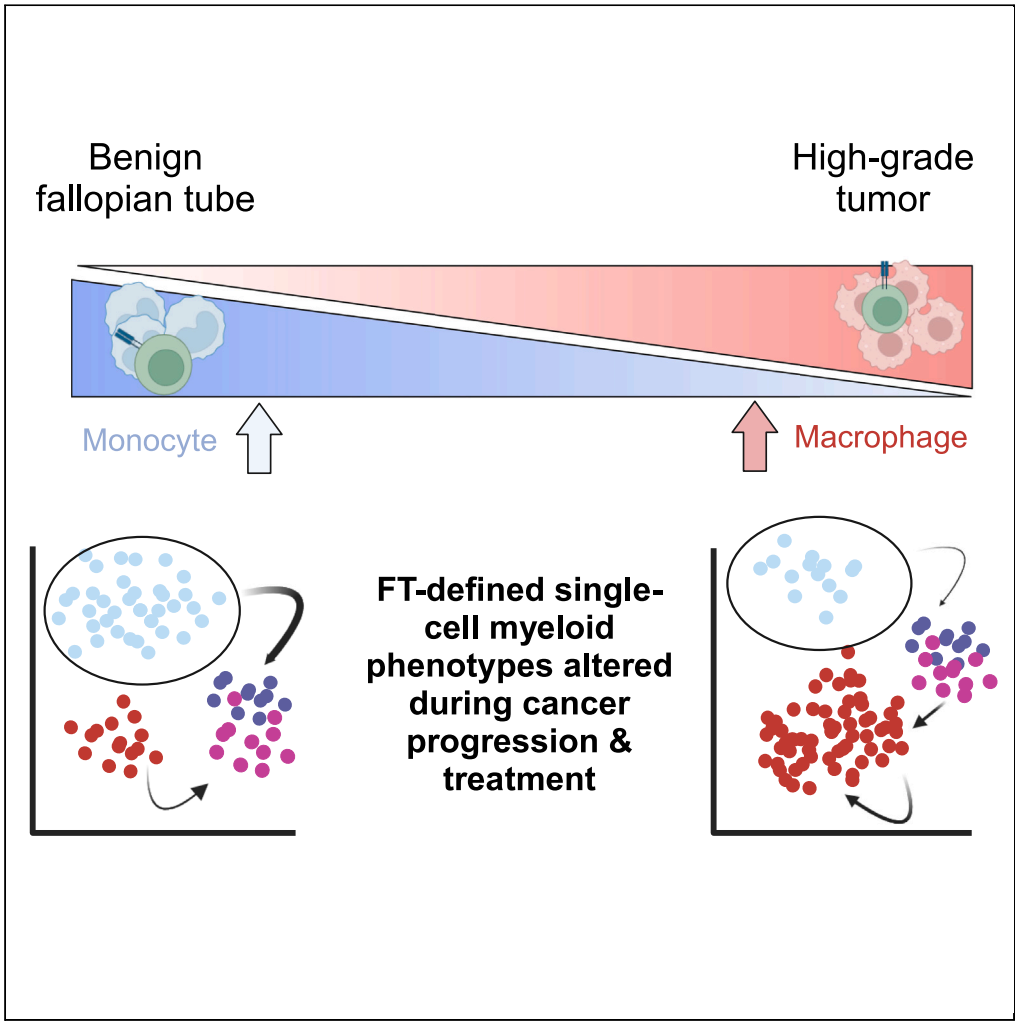

Joshua Brand, Marcela Haro, Xianzhi Lin, B.J. Rimel, Stephanie M. McGregor, Kate Lawrenson, Huy Q. Dinh

huy.dinh@wisc.edu

Highlights

Single cell transcriptomics identify the abundance of monocytes in human fallopian tubes

The macrophage-to-monocyte ratio is increased from normal to ovarian cancer state

Myeloid gene expression alters in patients with germline BRCA1 and with chemotherapy

Myeloid-stromal interactions differ in normal and high-grade serous ovarian cancer

Brand et al., iScience 27, 108990
March 15, 2024
https://doi.org/10.1016/j.isci.2024.108990

iScience

CellPress
OPEN ACCESS

Article

Fallopian tube single cell analysis reveals myeloid cell alterations in high-grade serous ovarian cancer

Joshua Brand,[1] Marcela Haro,[2,3] Xianzhi Lin,[2,3,4] B.J. Rimel,[2,3] Stephanie M. McGregor,[5,6] Kate Lawrenson,[2,3] and Huy Q. Dinh[1,6,7,8,*]

SUMMARY

Most high-grade serous ovarian cancers (HGSCs) likely initiate from fallopian tube (FT) epithelia. While epithelial subtypes have been characterized using single-cell RNA-sequencing (scRNA-Seq), heterogeneity of other compartments and their involvement in tumor progression are poorly defined. Integrated analysis of human FT scRNA-Seq and HGSC-related tissues, including tumors, revealed greater immune and stromal transcriptional diversity than previously reported. We identified abundant monocytes in FTs across two independent cohorts. The ratio of macrophages to monocytes is similar between benign FTs, ovaries, and adjacent normal tissues but significantly greater in tumors. FT-defined monocyte and macrophage signatures, cell-cell communication, and gene set enrichment analyses identified monocyte- and macrophage-specific interactions and functional pathways in paired tumors and adjacent normal tissues. Further reanalysis of HGSC scRNA-Seq identified monocyte and macrophage subsets associated with neoadjuvant chemotherapy. Taken together, our work provides data that an altered FT myeloid cell composition could inform the discovery of early detection markers for HGSC.

INTRODUCTION

A lack of early detection markers for high-grade serous ovarian cancers (HGSCs) has contributed to patients' poor clinical outcomes and stagnant survival rates over several decades.[1] Earlier data has provided pathological evidence of p53 signatures in lesions within the fallopian tubes (FT) of women with BRCA1/2 mutations who were at risk of HGSCs.[2–6] Emerging molecular data show that the majority of HGSCs likely arise from secretory cells at the fimbriated end of the fallopian tube (FT), including whole exome sequencing and copy number analysis[7–11] and single-cell RNA-Seq.[12,13] Altogether, it is important to characterize the FT tissue microenvironment to gain insight into the earliest stages of HGSC development. While significant efforts have been made to characterize the tumor microenvironment (TME) of HGSCs[14–19] and benign FT epithelia[12,13] using single-cell transcriptomics (scRNA-Seq), there remains a critical need to connect the single-cell landscape of stromal and immune subsets of human FT to HGSC.

Limited data have been reported on the extended heterogeneity of human FT immune cell subsets and their cell-cell interactions, which may influence HGSC development and patient outcomes. Previous studies used protein-panel-based technologies such as immunohistochemistry (IHC)[20] and flow cytometry[21–23] to profile human FT immune subsets with limited markers for phenotyping beyond those for cell type identification, such as macrophages, dendritic cells (DCs), and T cells/natural killer cells (T/NK cells). The heterogeneity of T/NK, myeloid, and stromal cells and their cell-cell interactions in FT remain incomplete in published scRNA-Seq analyses.[24] We therefore analyzed immune and stromal cell heterogeneity from scRNA-Seq of benign human FTs[24] and HGSC tumors and adjacent normal samples from >80 in-house and publicly available sources,[14–16,18,24–26] identifying 7 fibroblast/stromal, 6 T/NK, and 7 myeloid cell subsets with distinct gene, pathway, and regulatory network signatures. Further examination of single-cell derived transcriptomic signatures reveals associations with molecular subtypes in bulk transcriptome data from The Cancer Genome Atlas (TCGA). Lastly, we show a significant macrophage-to-monocyte ratio shift in tumors compared to benign FT and transcriptional changes in FTs from women with *BRCA*1/2 mutations and patients with HGSC treated with chemotherapy. These results provide a better understanding of human FT heterogeneity and its implications for HGSC outcomes.

[1]McArdle Laboratory for Cancer Research, Department of Oncology, School of Medicine and Public Health, University of Wisconsin – Madison, Madison, WI 53705, USA
[2]Women's Cancer Research Program at the Samuel Oschin Comprehensive Cancer Center, Cedars-Sinai Medical Center, Los Angeles, CA 90048, USA
[3]Division of Gynecologic Oncology, Department of Obstetrics and Gynecology, Cedars-Sinai Medical Center, Los Angeles, CA 90048, USA
[4]RNA Biology Group, Division of Natural and Applied Sciences and Global Health Research Center, Duke Kunshan University, Kunshan 215316, Jiangsu Province, China
[5]Department of Pathology and Laboratory Medicine, University of Wisconsin – Madison, Madison, WI 53705, USA
[6]University of Wisconsin Carbone Cancer Center, University of Wisconsin School of Medicine and Public Health, Madison, WI 53705, USA
[7]Department of Biostatistics and Medical Informatics, School of Medicine and Public Health, University of Wisconsin – Madison, Madison, WI 53705, USA
[8]Lead contact
*Correspondence: huy.dinh@wisc.edu
https://doi.org/10.1016/j.isci.2024.108990

RESULTS

Single-cell RNA-sequencing analysis of non-epithelial cell compartment in human fallopian tubes

To characterize the cellular and molecular characteristics of the human FT tissue microenvironment, we reanalyzed the non-epithelial cell compartment from our previously published scRNA-Seq,[13] which included 45,654 non-epithelial cells. Here, we focus on immune and stromal heterogeneity and compare our subsets to a recently published, independent scRNA-Seq study.[24] In addition, we generated in-house and utilized additional publicly available scRNA-Seq data from adjacent non-malignant tissues and tumors from patients with HGSCs (total: n = 88 samples across 58 donors, Figure 1A; Table S1). We further clustered 9,759 stromal cells, 32,598 T/NK cells, and 1,850 myeloid cells from 12 FT samples[13] (Figures 1B, S1A, and S1B) and identified 7 myeloid, 4 T cell, 2 NK cell, 4 fibroblast, 2 pericyte, and 1 smooth muscle cell subsets (STAR Methods). In addition, using label transfer,[27] we were able to identify all annotated cell subsets in an independent scRNA-Seq dataset from 4 benign FT donors[24] (Figures S1C and S1D). When comparing benign FT and ovarian epithelia to HGSC tumors, we quantify a higher Spearman correlation coefficient between HGSC tumor cells and FT epithelial cells (rho = 0.67), especially secretory cells (rho = 0.71) compared to the ovarian epithelial cells (rho = 0.56) (Figure S1E), consistent with previous scRNA-Seq.[12,13]Our analysis identifies greater myeloid diversity measured by an entropy-based scoring method, Rogue[28] compared to T/NK cell clusters, despite being just 5% as frequent as T/NK cells in our scRNA-Seq (Figure S1F) samples. Additionally, we calculated the number of unique statistically differentially expressed (DE) genes (Figure S1G), showing that myeloid cells consistently had more DE genes per cluster and justifying the decision to maintain more myeloid clusters than T/NK cells. In our stromal subsets, we identify 3 fibroblast subsets and a small cluster with a myeloid-like gene signature, with potential antigen-presenting functions as recently identified in multiple tissue types.[29,30] Due to the limited number of captured cells in the scRNA-Seq, we did not further cluster other cell types, such as B and endothelial cells.

Myeloid cell heterogeneity and plasticity in human fallopian tubes

Myeloid cell diversity in high-grade serous ovarian cancers was recently described with multifaceted, functional gene signatures in distinct tumor microenvironments (TME).[19] We reasoned that an in-depth transcriptional characterization of FT myeloid cells would help us identify a link between the myeloid microenvironment of HGSC and FTs, the tissue of origin for most HGSC tumors. Our clustering analysis (STAR Methods) defined 4 classical ($CD14^+$, $CD16^-$) monocyte (Mono) subsets (Mono_CCL4hi, Mono_CCL4lo, Mono_HSP, and Mono_VCAN/CFD), 1 nonclassical $CD16^+$ (encoded by *FCGR3A*) monocyte subset (Mono_CD16), 1 DC (DC_CLEC10A), and 1 macrophage (Mac) subset (Mac_C1Q) (Figure 2A) that were shared across 9 FT samples (3 samples were not included due to low cell counts) (Figure S1B). Downstream analysis including differential gene expression, gene set enrichment analysis using JASMINE,[31] and gene regulatory network analysis from SCENIC[32] (STAR Methods) defined distinct gene signatures (Figures 2B–2D) in the 7 myeloid subsets and supported our cell type annotations. We used representative markers to annotate myeloid subsets, including 4 classical monocyte subsets with variable expression levels of *CCL4*, a chemoattractant of T and myeloid cells that was found to correlate with $CD8^+$ and FOXP3+ T cell infiltration in HGSCs.[33] Other markers include the proteoglycan versican (*VCAN*) and heat shock proteins (HSPs), which describes stress-responsive monocytes.[34] Macrophages, which expressed complement complex genes *C1QA/B* as well as *TREM2* were transcriptionally distinct from monocytes by their lack of *FCN1* and *S100A8/9* expression as well as chemoattractant and inflammatory molecules such as *IL1A*, *CXCL2/3/8*, and *CCL20*. JASMINE pathway analysis using Gene Ontology Biological Process (GO: BP) revealed gene sets enriched for classical monocytes (inflammatory response, leukocyte chemotaxis), HSP+ monocytes (protein folding), non-classical $CD16^+$ monocytes (interferon-inducible pathways), antigen-presenting pathways in macrophages and DCs and lipid metabolism pathways unique to macrophages (Figure 2C). Gene regulatory network analysis performed with SCENIC[32,35] (STAR Methods) showed *BHLHE41* and *MAF* regulons enriched within macrophages; both negative regulators of macrophage proliferation and activation.[36,37] *EHF* and *ETV3* regulons were also active, likely reflecting dendritic cell differentiation programs,[38,39] and *IRF4*, a DC-lineage transcription factor that promotes TH2 polarization[40] (Figure 2D).

To test how potential monocytic developmental trajectories in human FT correlates with our defined regulatory networks, we paired SCENIC results with diffusion maps[41] and Monocle's graph-based pseudotime.[42] Diffusion map analysis suggested two distinct diffusion components, one associated with MHC-II antigen presenting genes and the second with inflammatory cytokine expression (Figures 2E and S2A). Monocle supported the inferred pseudotime trajectory from classical $CD14^+$ monocytes to more matured monocytic cell types (dendritic cells, macrophages) or distinct monocyte states (HSP/*VCAN* monocytes and non-classical $CD16^+$ monocytes) supported by the enrichment score of SCENIC regulons. The top correlated genes with each diffusion component indicated how monocytic cells might function differently during their maturation. We ranked the top 10 correlating genes with each diffusion component (Figure S2A) to indicate how monocytic cells might function distinctly during their maturation. For instance, enrichment scores derived from the average expression in single-cell clusters suggested cytokine/interleukin genes were enriched with monocytes while HLA gene sets were enriched within macrophages and DCs.

Next, we used FT-defined myeloid cell signatures to evaluate their enrichment in 394 HGSC samples from TCGA[43] and found that signatures of more mature monocytic subsets such as *VCAN*+ monocytes and macrophages were most enriched for immunoreactive and mesenchymal HGSC subtypes (Figure S2B, STAR Methods). Together, our analysis revealed extensive heterogeneity of myeloid cells in human FTs and suggested a phenotypic change in myeloid cells that may be relevant in HGSCs.

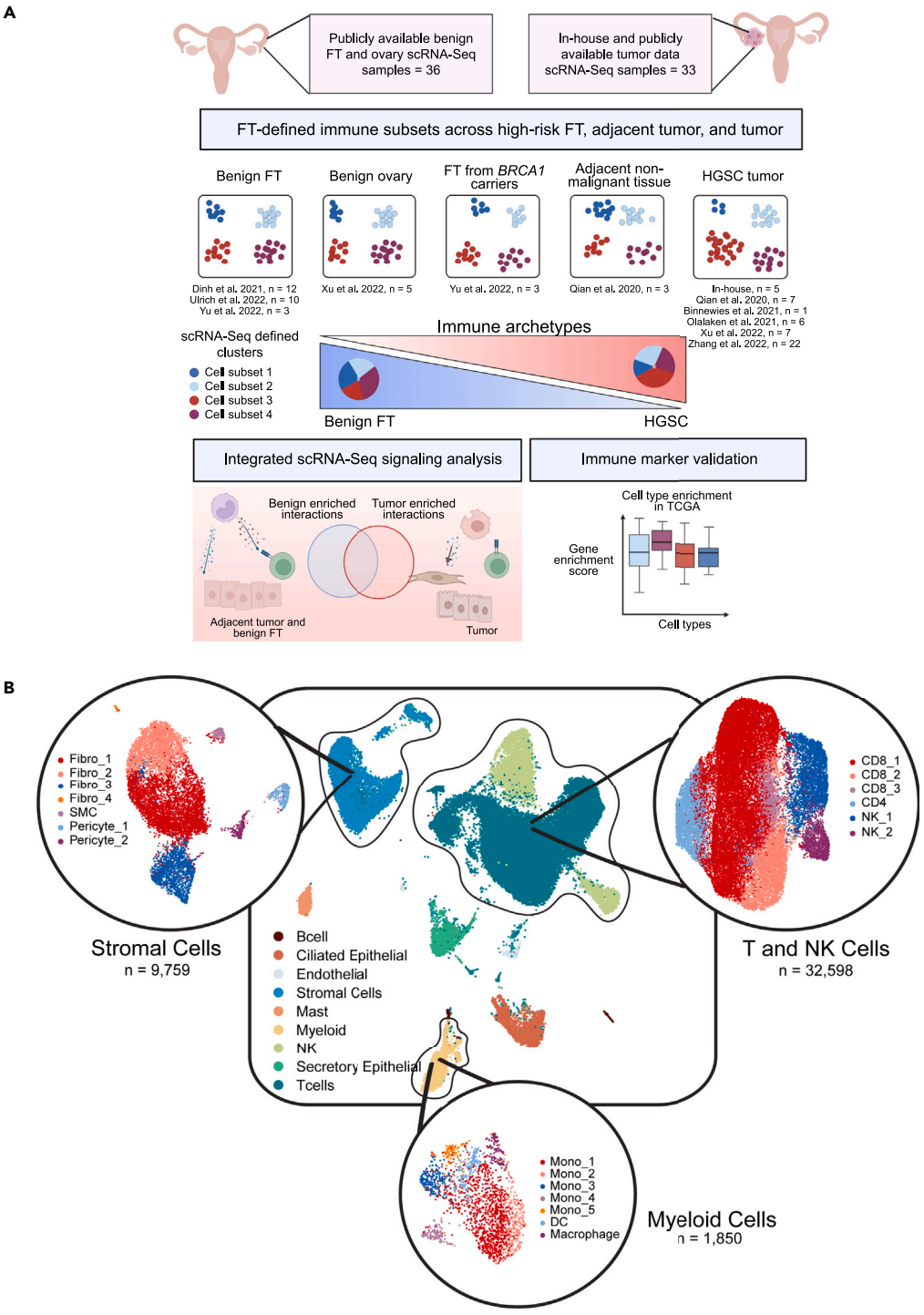

Figure 1. Integrated scRNA-Seq analysis of human fallopian tubes to identify immune features of HGSC progression

(A) Bioinformatics analysis of 88 scRNA-Seq samples, including in-house and publicly available data, identifies heterogeneity and interactions of immune and stromal cells in FTs and their alterations across adjacent normal tumors, benign ovaries, and HGSCs. (Created with Biorender.com).

(B) Transcriptional heterogeneity of stromal, T/NK, and myeloid cell subsets from 12 FT samples[13] served as a reference for further analysis across relevant tissue and sample types. Mono: monocytes, SMC: smooth muscle cells, NK: natural killer cells, DC: dendritic cells.

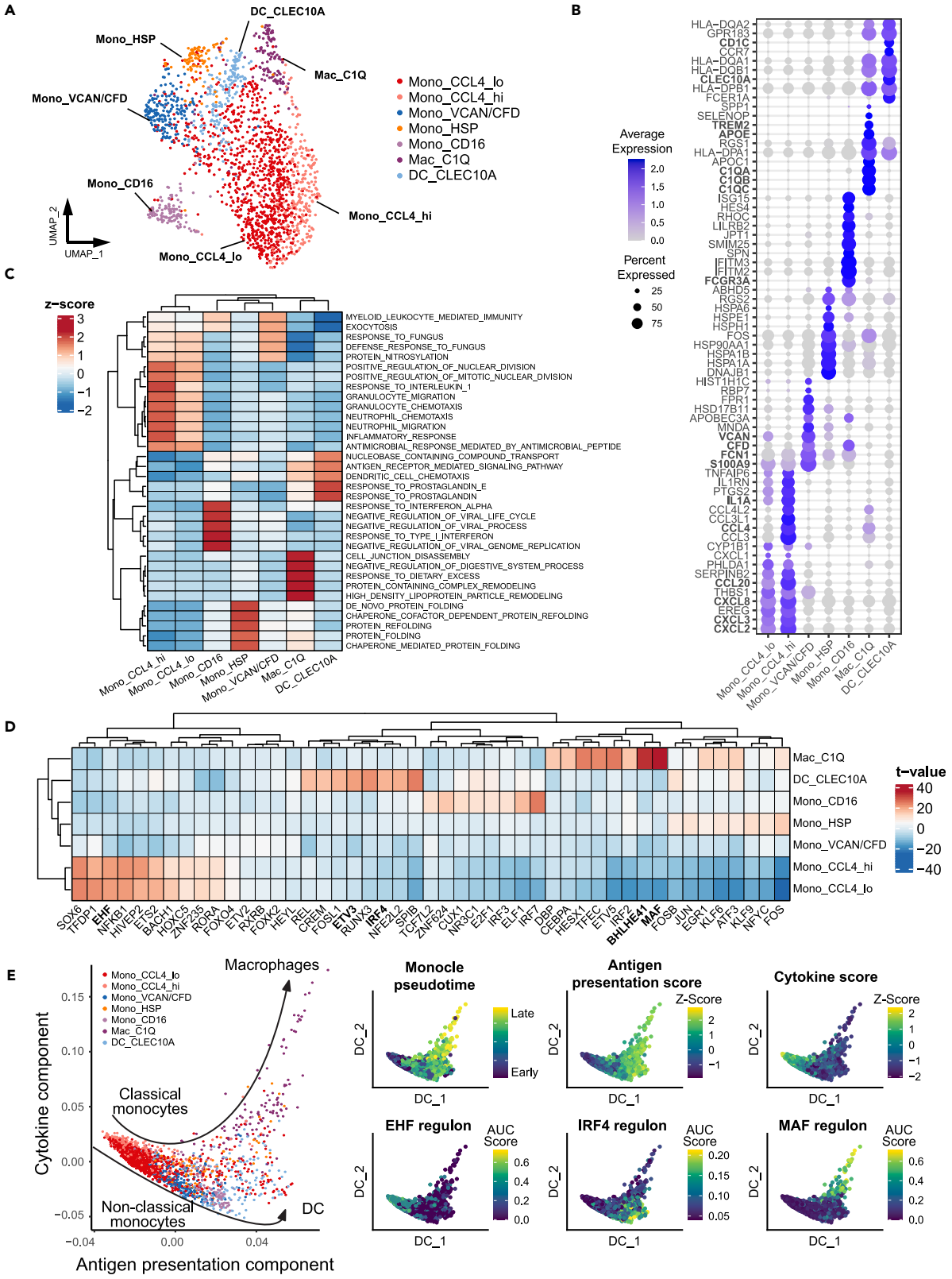
A
DC_CLEC10A
Mono_HSP
Mac_C1Q
Mono_VCAN/CFD
Mono_CD16
Mono_CCL4_hi
Mono_CCL4_lo
UMAP_2
UMAP_1
Mono_CCL4_lo
Mono_CCL4_hi
Mono_VCAN/CFD
Mono_HSP
Mono_CD16
Mac_C1Q
DC_CLEC10A
B
Average Expression
2.0
1.5
1.0
0.5
0.0
Percent Expressed
25
50
75
HLA-DQA2
GPR183
CD1C
CCR7
HLA-DQA1
HLA-DQB1
CLEC10A
HLA-DPB1
FCER1A
SPP1
SELENOP
TREM2
APOE
RGS1
HLA-DPA1
APOC1
C1QA
C1QB
C1QC
ISG15
HES4
RHOC
LILRB2
JPT1
SMIM25
SPN
IFITM3
IFITM2
FCGR3A
ABHD5
RGS2
HSPA6
HSPE1
HSPH1
FOS
HSP90AA1
HSPA1B
HSPA1A
DNAJB1
HIST1H1C
RBP7
FPR1
HSD17B11
APOBEC3A
MNDA
VCAN
CFD
FCN1
S100A9
TNFAIP6
IL1RN
PTGS2
IL1A
CCL4L2
CCL3L1
CCL4
CCL3
CYP1B1
CXCL1
PHLDA1
SERPINB2
CCL20
THBS1
CXCL8
EREG
CXCL3
CXCL2
Mono_CCL4_lo
Mono_CCL4_hi
Mono_VCAN/CFD
Mono_HSP
Mono_CD16
Mac_C1Q
DC_CLEC10A
C
z-score
3
2
1
0
−1
−2
MYELOID_LEUKOCYTE_MEDIATED_IMMUNITY
EXOCYTOSIS
RESPONSE_TO_FUNGUS
DEFENSE_RESPONSE_TO_FUNGUS
PROTEIN_NITROSYLATION
POSITIVE_REGULATION_OF_NUCLEAR_DIVISION
POSITIVE_REGULATION_OF_MITOTIC_NUCLEAR_DIVISION
RESPONSE_TO_INTERLEUKIN_1
GRANULOCYTE_MIGRATION
GRANULOCYTE_CHEMOTAXIS
NEUTROPHIL_CHEMOTAXIS
NEUTROPHIL_MIGRATION
INFLAMMATORY_RESPONSE
ANTIMICROBIAL_RESPONSE_MEDIATED_BY_ANTIMICROBIAL_PEPTIDE
NUCLEOBASE_CONTAINING_COMPOUND_TRANSPORT
ANTIGEN_RECEPTOR_MEDIATED_SIGNALING_PATHWAY
DENDRITIC_CELL_CHEMOTAXIS
RESPONSE_TO_PROSTAGLANDIN_E
RESPONSE_TO_PROSTAGLANDIN
RESPONSE_TO_INTERFERON_ALPHA
NEGATIVE_REGULATION_OF_VIRAL_LIFE_CYCLE
NEGATIVE_REGULATION_OF_VIRAL_PROCESS
RESPONSE_TO_TYPE_I_INTERFERON
NEGATIVE_REGULATION_OF_VIRAL_GENOME_REPLICATION
CELL_JUNCTION_DISASSEMBLY
NEGATIVE_REGULATION_OF_DIGESTIVE_SYSTEM_PROCESS
RESPONSE_TO_DIETARY_EXCESS
PROTEIN_CONTAINING_COMPLEX_REMODELING
HIGH_DENSITY_LIPOPROTEIN_PARTICLE_REMODELING
DE_NOVO_PROTEIN_FOLDING
CHAPERONE_COFACTOR_DEPENDENT_PROTEIN_REFOLDING
PROTEIN_REFOLDING
PROTEIN_FOLDING
CHAPERONE_MEDIATED_PROTEIN_FOLDING
Mono_CCL4_hi
Mono_CCL4_lo
Mono_CD16
Mono_HSP
Mono_VCAN/CFD
Mac_C1Q
DC_CLEC10A
D
t-value
40
20
0
−20
−40
Mac_C1Q
DC_CLEC10A
Mono_CD16
Mono_HSP
Mono_VCAN/CFD
Mono_CCL4_hi
Mono_CCL4_lo
SOX6
TFDP1
EHF
NFKB1
HIVEP2
ETS2
BACH1
HOXC5
ZNF235
RORA
FOXO4
ETV2
RXRB
FOXK2
HEY1
REL
CREM
FOSL1
ETV3
RUNX3
IRF4
NFE2L2
SPIB
TCF7L2
ZNF624
CUX1
NR3C1
E2F1
IRF3
ELF1
IRF7
DBP
CEBPA
HESX1
TFEC
ETV5
IRF2
BHLHE41
MAF
FOSB
JUN
EGR1
KLF6
ATF3
KLF9
NFYC
FOS
E
Mono_CCL4_lo
Mono_CCL4_hi
Mono_VCAN/CFD
Mono_HSP
Mono_CD16
Mac_C1Q
DC_CLEC10A
Macrophages
Classical monocytes
Non-classical monocytes
DC
Cytokine component
Antigen presentation component
0.15
0.10
0.05
0.00
−0.05
−0.04
0.00
0.04
Monocle pseudotime
Late
Early
Antigen presentation score
Z-Score
Cytokine score
Z-Score
EHF regulon
AUC Score
IRF4 regulon
AUC Score
MAF regulon
AUC Score
DC_1
DC_2

Figure 2. Myeloid cell heterogeneity in human FTs shows a higher diversity of monocytes than macrophages and dendritic cells

(A) UMAP and clustering of integrated myeloid cells identify 4 classical monocyte subsets (*CD14*, *FCGR3A*-), 1 subset of non-classical monocytes (*CD14*, *FCGR3A+*), a subset of type 2 dendritic cells (*CD1C*, *CLEC10A*), and macrophages (*APOE*, *TREM2*).

(B) Representative gene signatures of myeloid subsets presented by DotPlot; values show z-scaled RNA expression across clusters. Extended differential expression analysis in Table S2.

(C) Gene set enrichment analysis of top-scoring Biological Processes Gene Ontology (GO: BP) for myeloid subsets. Values shown are z-scores of Jasmine's odds ratio test across clusters.

(D) Gene regulatory network analysis using SCENIC shows regulon scores enriched for each myeloid subset. Values plotted are derived from linear models using one cluster vs. the remaining and extracting the t-values for each model (STAR Methods).

(E) Diffusion map of myeloid cells calculated using the top 2000 variable features. Monocle3 pseudotime, gene set scores, and SCENIC AUC scores (STAR Methods) were overlaid on the 1st two diffusion components.

Macrophage-to-monocyte ratio is distinct in the fallopian tube, adjacent normal tissues, and high-grade serous ovarian tumors

Previous flow cytometry and scRNA-Seq analyses did not annotate monocyte subset in FTs[22,24]; however, their signatures were identified in HGSC scRNA-Seq[19] that correlated with T/NK cell phenotypes. Since monocyte signatures (*S100A8/9*, *FCN1*, *VCAN*) from circulating blood[44] and HGSC tumor[19] are consistent with our FT-defined monocytes, we asked if we could identify monocytes in independent samples of healthy FT scRNA-Seq[24] (Figures S3A and S3B). Our clustering analysis recovers abundant monocytes with similar marker genes as identified in our FT samples (*S100A8/9*, *FCN1*, *TREM2*, *CD1C*) and consistently differentiated macrophages, monocytes, and DCs from each other. Using label transfer,[27] we show that monocyte subsets are retained in other previously published data[24] (Figures S3C and S3D). We observed that *S100A9* and *FCN1* consistently separate monocytes from dendritic cells and *TREM2+ C1QA/B* macrophages. The comparatively low abundance of macrophages relative to monocytes in benign FT scRNA-Seq datasets led us to evaluate their proportions in adjacent normal tissues compared to HGSC tumors from the same patients. We reanalyzed two independent scRNA-Seq datasets, one with paired adjacent normal and tumor from[14] and another with 5 benign ovarian tissues and 7 HGSCs from Xu et al.[18] to compare myeloid cell composition across disease conditions and tissue types. The addition of these datasets brought our sample size to 26 total HGSC samples, which were compared benign FT (n = 22), benign ovary (n = 5), and adjacent normal samples (n = 3), and low-grade ovarian cancer samples (n = 4). We found a significantly elevated macrophage-to-monocyte ratio in HGSC tumors compared to benign FT tissues (3.40-fold increase, FDR adjusted p value = $3.6x10^{-6}$) (Figures 3A and 3B), while the difference between adjacent, non-malignant tissue, or benign ovary compared to healthy FT tissue are less pronounced (1.90, and 1.94-fold increase, respectively) and were not found to be statistically significant (FDR adjusted p values = 0.19, 0.50). The macrophage-to-monocyte ratio was not significantly different between adjacent normal tissues compared to that in low-grade ovarian cancer in our newly generated scRNA-Seq (Figure 3B). Taking advantage of the recent availability of published scRNA-Seq datasets, we reanalyzed additional HGSC tumor scRNA-Seq[15,16,18] and, on average, found a higher macrophage-to-monocyte ratio in HGSC TME from different datasets (total n = 26 HGSC samples).

To identify the potential difference in myeloid cells' functions in adjacent normal and benign tissue, we used scRNA-Seq of adjacent normal (n = 3) and HGSCs (n = 7).[14] JASMINE GO: BP pathway analysis showed marked differences in monocytes in adjacent tissues compared to tumors, including the enrichment of anti-angiogenic pathways in adjacent monocytes compared to tumors (negative regulation of endothelial cell chemotaxis FDR adjusted p value = $1.58\ x10^{-25}$ and positive regulation of endothelial cell apoptotic process FDR adjusted p value = $4.10x10^{-21}$) (Figure 3C). In contrast, tumor-associated monocytes were significantly enriched in metabolic-related pathways (High-density lipoprotein particle remodeling FDR adjusted p value = $4.20\ x10^{-14}$ and NAD metabolic process FDR adjusted p value = $1.33\ x10^{-9}$) compared to adjacent normal monocytes, and similar to tumor-associated macrophages (TAMs). We also observed shifted metabolic pathways in TAMs, supporting their change in energy demands compared to adjacent tissue. Notably, we see a reduced reliance on oxygen for metabolism demonstrated with a significantly lower JASMINE score for the "oxygen transport" pathway (FDR adjusted p value = $5.11\ x10^{-265}$) and "acetyl coenzyme-A biosynthesis" pathway (FDR adjusted p value = $9.03x10^{-211}$), which is an essential precursor for oxidative phosphorylation.

Fallopian tube-defined cell-cell interactions of monocytes and macrophages are correlated in adjacent normal and matched high-grade serous ovarian cancer tumors

Since the phenotypes of monocytes and macrophages are associated with different types of HGSC TMEs,[19] we asked if the cell-cell interactions of monocytes and macrophages with other cell types in FTs are altered in tumor compared to benign tissue (FT and adjacent normal) (Figure 3B). To test this, we further identified 6 T/NK cell subsets, including 3 $CD8^+$ cell subsets, 2 NK cell subsets, and 1 CD4 subset with distinct gene signatures (Figures S4A and S4B). Among those, scRNA-Seq-derived signature scores identified T/NK subsets were highest in immunoreactive subtypes in most subsets, but particularly in NK cells. (Figure S4C). Further sub-clustering did not obtain more subsets with sufficient DE genes for T cell subset annotation with conventional phenotypic markers, including T memory and helper subtypes (Figure S4D).

To evaluate the cell-cell interaction (CCI) signals from scRNA-Seq, we used Cellchat[45] ligand-receptor database and quantified the significant interactions across major subtypes in our defined human FT atlas (Figure 4A). CellChat's permutation test identified 121 significant ligand-receptor pairs with monocytes/macrophages as a sender cell type, in which 83 (68.6%) were shared between macrophages and monocytes, while 22 (18.2%) and 16 (13.2%) specifically identified from either macrophages or monocytes, respectively (Figures 4B and 4C). The dominant signaling pathways of macrophage CCIs were *CLEC2B* and TNF signaling, which engages the *KLRB1* and TNFR receptors, known for self-recognition and negative regulation of T/NK cell activation[46,47] and inflammation, respectively. Other macrophage CCIs, including *PDGFB-PDGFRA/B* between macrophages and stromal cells, were reported in HGSC tumors with reactive stroma and poor prognosis.[48]

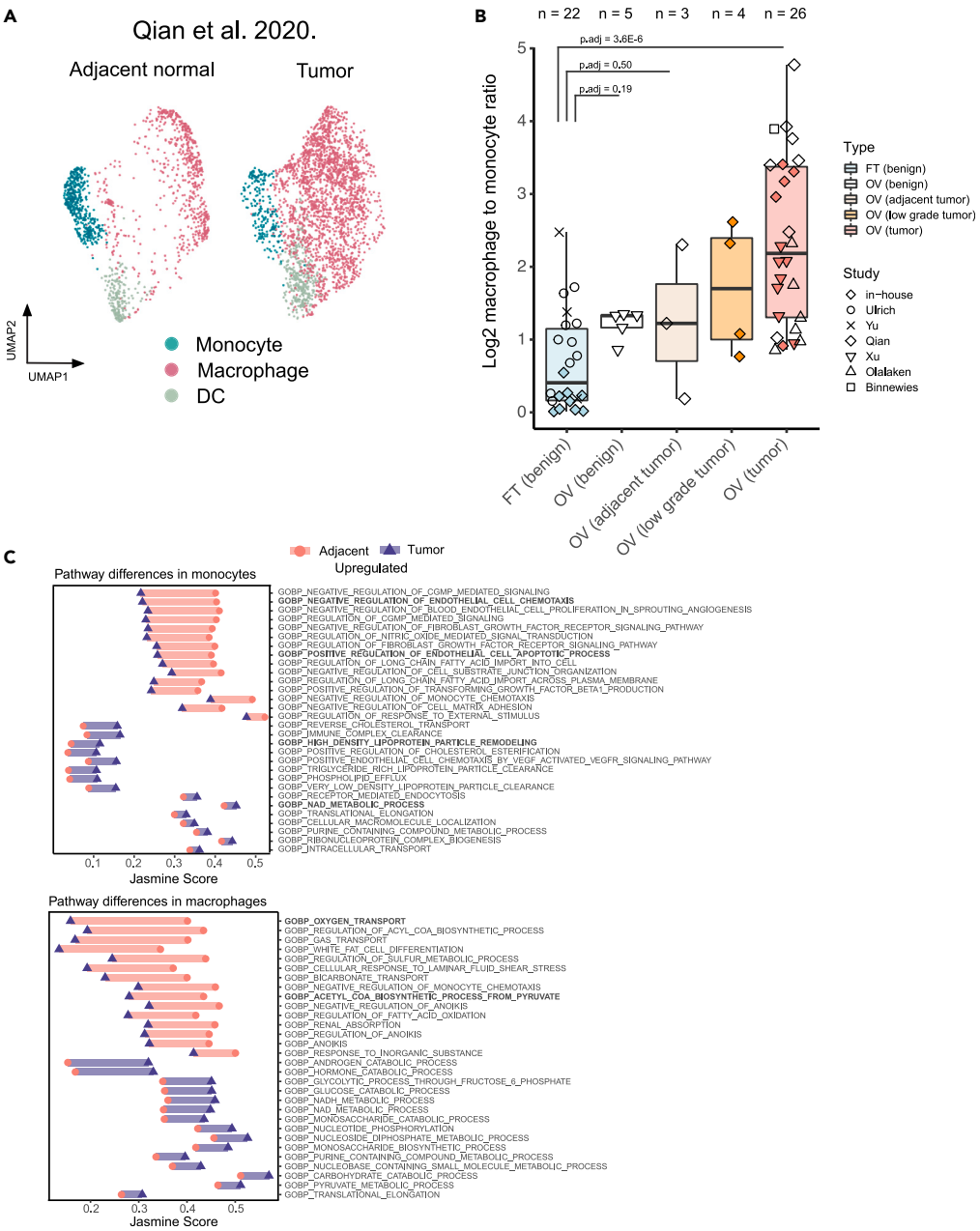

Figure 3. Analysis of macrophage-to-monocyte ratio across tissue types and conditions

(A) UMAP and clustering of myeloid cells from[14] data[14] shows the enrichment of macrophages relative to monocytes. (n = 3 samples per group, 2 patients).

(B) The log2 macrophage-to-monocyte ratio across benign FT, benign ovary, adjacent normal tumor, low-grade, and HGSC tumor (FDR-adjusted p value, two-sided pairwise Wilcox test). The n values correspond to individual samples, in which multiple could be derived from an individual patient (Table S1).

(C) Jasmine scores (GO:BP) were calculated for macrophages and monocytes across adjacent normals and tumors from Qian et al.[14] (n = 3 samples, each). scRNA-Seq (panel A). Significant pathways (two-sided t-test, FDR-adjusted p value <0.01) were ranked by fold change between microenvironments and the Jasmine scores plotted.

On the other hand, monocyte CCIs included epiregulin (*EREG*), which has potential interactions with stromal cells through *EGFR*, or ciliated epithelial cells through HER family receptors *ERBB2* and *ERBB4*, reported in low-grade serous ovarian cancers.[49] Another relevant monocyte interaction, *THBS1-CD47*, showed a reduction in angiogenesis and increased tumor rejection in a xenotransplant model, suggesting its pro--tumoral effects.[50] Next, we performed the same CCI analysis using macrophages and monocytes as receiving populations (Figures S5A and S5B), which highlighted the increased diversity in macrophage receptor use such as with *LRP1*, *AXL*, *CSF1R*, *HAVCR2*, *C3AR1* when compared to monocytes.

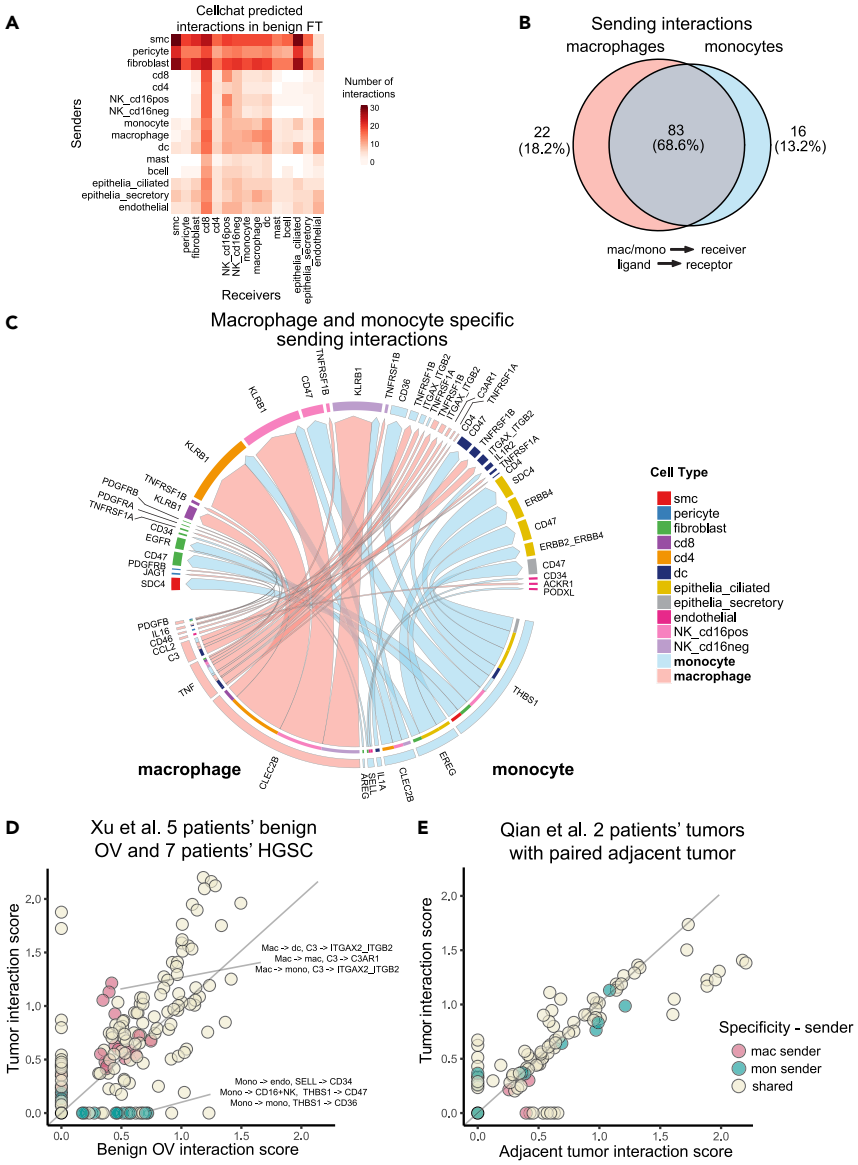

Figure 4. Cell-cell interaction analysis of monocytes and macrophages in FTs with other cell types

(A) Frequency of significant CCIs in human FTs (12 samples[30]) identified by CellChat's permutation test[45] (STAR Methods). SMC: smooth muscle cell, DC: dendritic cell, CD8: $CD8^+$ T cell, CD4: CD4+T cell.

(B) Comparison of monocyte- and macrophage-specific sending CCIs in human FTs.

(C) Circos plot of monocyte- and macrophage-specific CCIs. Arrow width represents Cellchat's scaled interaction scores.

(D) CCI coexpression scores of monocyte- and macrophage-specific CCIs in tumor and benign ovary.[18] Each point represents a CCI score (STAR Methods). Interactions are represented as sender cell type -> receiver cell type, ligand -> receptor. Mac: macrophage, dc: dendritic cell, mono: monocyte, NK: natural killer cell.

(E) CCI coexpression scores of monocyte- and macrophage-specific CCIs in tumor and adjacent normal samples.[14] Interactions are represented as sender cell type -> receiver cell type, ligand -> receptor.

Since we observed the difference in the macrophage-to-monocyte ratio in samples compared to tumors, we asked if the FT-defined CCIs expressed differently in adjacent normal and tumors. To do so, we compared co-expression CCI scores (STAR Methods) of the FT-defined monocyte- and macrophage-specific and shared CCIs in adjacent normal and tumor samples from two independent scRNA-Seq datasets.[14,18] The co-expression of our CCI scores positively correlated with CellChat's communication probabilities (Figure S5C), which allowed us to identify cross-tissue CCIs between benign, adjacent normal, and tumor tissues. We observed that interactions with monocytes as senders were enriched in the benign ovary,[18] with 11 monocyte-specific positive scored interactions in the benign ovary and 2 in tumors, whereas most interactions with macrophages as senders were similar between normal and tumor (Figure 4D). In a second dataset we observed a high

correlation between these interactions, but not in a cell type-specific manner[14] (Figure 4E). The receiving signals were also consistently correlated between these datasets (Figures S5D and S5E), indicating that tumor microenvironment and cell-cell interactions may be intrinsic to their cell identities based on their high correlation across different tissues.

Monocyte and macrophage diversity in patients with germline *BRCA1* mutations and patients with high-grade serous ovarian cancer treated with chemotherapy

We identified the macrophage-to-monocyte ratio changes as potentially linked with disease progression. Next, we wanted to evaluate this ratio using FT scRNA-Seq from patients with *BRCA1* germline mutations,[25] who are high risk of developing HGSCs. We used marker genes consistent with our 12 sample FT reference to identify myeloid cell types (Figures S6A and S6B) using representative genes (LYZ for pan-myeloid cells, FCN1 for monocytes, and C1QB for macrophages, consistent with our FT data). We observed an increase in macrophage-to-monocyte ratio in FT of *BRCA1* germline mutation (p value = 0.7, two-sided Wilcox test, N = 3 vs. 3). (Figure 5A). Differential gene expression showed an increased in the chemokines *CCL3* and *CXCL2/8*, first identified from our FT monocyte subsets, in macrophages and monocytes of BRCA1 FT samples, and decreased the expression of heat shock protein (HSP) genes in BRCA samples (Figure 5B). The data indicated a potential of change in macrophage-to-monocyte ratio in FT of HGSC high-risk patients compared to healthy FT but remains limited due to the small sample size.

We were also curious how the macrophage-to-monocyte ratio may change in patients with HGSC upon treatment. We reanalyzed a publicly available treatment-naïve scRNA-Seq dataset from 11 patients taken before and after neoadjuvant chemotherapy treatment[26] (Figure S6C). Our myeloid cell clustering identified 2 populations of monocytes, 5 populations of macrophages, and 2 dendritic cell subsets (Figures 5C and 5D) with distinct gene signatures resembling those defined in our FT analysis (*CCL3/4*, *CXCL3*, *HSPA1A*, *FCN1*, *CCL20*, *C1QA*). Overall, chemotherapy's effect on the macrophage-to-monocyte ratio is uncertain. There is no significance when using all samples, including those with poor cell recovery, which are likely more variable (p value = 0.456). However, after removing donors with fewer than 50 total myeloid cells combined (N = 2), we see a 1.45-fold increase in the log2 ratio (p value = 0.0485). More samples are needed to determine the reproducibility of this effect. Additionally, we observed three subsets that significantly increased in proportion after treatment, including macrophages expressing *APOE*, *APOC1*, and complement components (C1Qs) (cluster 1, FDR adjusted p value = 0.045), HSP+ stress-related macrophages (cluster 6, FDR adjusted p value = 0.041), and classical monocytes (cluster 8, FDR adjusted p value = 0.011), that were most similar to the early FT-defined monocyte subsets (Figure 5E). Several subsets of monocyte and macrophage subpopulations are changed in HGSC as expected (Figure S6D), despite the uncertain impact on the ratio of macrophage-to-monocytes. We also note the increased complexity of myeloid cell diversity in the TME, especially within macrophages relative to benign tissue.

Stromal-immune cell interactions in human fallopian tubes

Since stromal cell-cell interactions were predicted to be the most frequent sending cell types inferred in FT scRNA-Seq, (Figure 4A), we asked to what extent their interactions with immune cells differ between normal FTs and HGSC tumors. To do so, we sub-clustered the stromal cell compartment (one sample was removed due to low cell count, STAR Methods), which identified three fibroblast subsets, two pericyte populations, and one smooth muscle cell (SMC) subset (Figure 6A) with distinct gene expression signatures, including complement genes (*C7*, *C3*, *CFD*) and cytokine/chemokine expression (*CXCL8*, *IL6*) (Figure 6B). We named the subsets with representative markers except for SMCs, which was comprised of one subset. F_RASD1 fibroblasts were suspected to be less differentiated/activated with high regulon activity of stemness markers *SOX4* and *TWIST2* from SCENIC (Figure S7A).[51] Smooth muscle and pericyte populations could be characterized by the differential expression of cell adhesion molecules (*MCAM*), *RGS5* (pericyte markers), *MYH11*, and *ZCCHC12* as smooth muscle cell markers (Figure S7B). Among those subsets, we found that F_C7 fibroblasts, marked by high expression of complement *C7* and SMC signature scores, were enriched in the TCGA HGSC mesenchymal subtype, known to have the worst survival outcomes (Figure 6C). Next, we used cancer-associated fibroblast (CAF) signatures from HGSC scRNA-Seq[17,19] to evaluate FT stromal subsets. We find complement expression (*CFD*) and other genes (*DPT*, *MGP*, and *CXCL12*) similar to inflammatory fibroblasts described in HGSCs[19] were enriched in our F_C7 subset relative to other stromal cells. (Figure S7C). CCI analysis using CellChat identified interactions between stromal subsets and immune receiver cells, particularly through *CD44*, *CD47* and integrins (Figure S7D). Most CCIs from fibroblast to immune cells were shared between our three fibroblast subsets (80%), though F_C7 fibroblasts have 22 CCIs not shared with other fibroblast subsets (12% of all stromal to immune interactions) (Figure 6D). Notably, fibroblast to myeloid signaling, including *C3* to *C3AR1*, associated with immunosuppression and cancer cell proliferation,[52] and *C3* to *ITGAX* and *ITGB2*, were among these (Figure S7D). *FN1* interactions, which were defined from our C7 expressing fibroblasts show interactions with diverse immune cell subsets and were predicted to have higher ligand-receptor co-expression in tumor relative to benign tissue from 2 independent cohorts (Figures 5E and 5F). Altogether, we reported a diversity of stromal cell subsets in human FTs, with distinct gene expression profiles and subsets that may contribute to distinct interactions enriched in HGSCs.

DISCUSSION

This study characterizes the diversity of non-epithelial compartments in benign FTs, especially immune cells and cell-cell interactions which was not fully described from recent scRNA-Seq. The defined single-cell transcriptional landscape of FT immune cells showed a greater extent

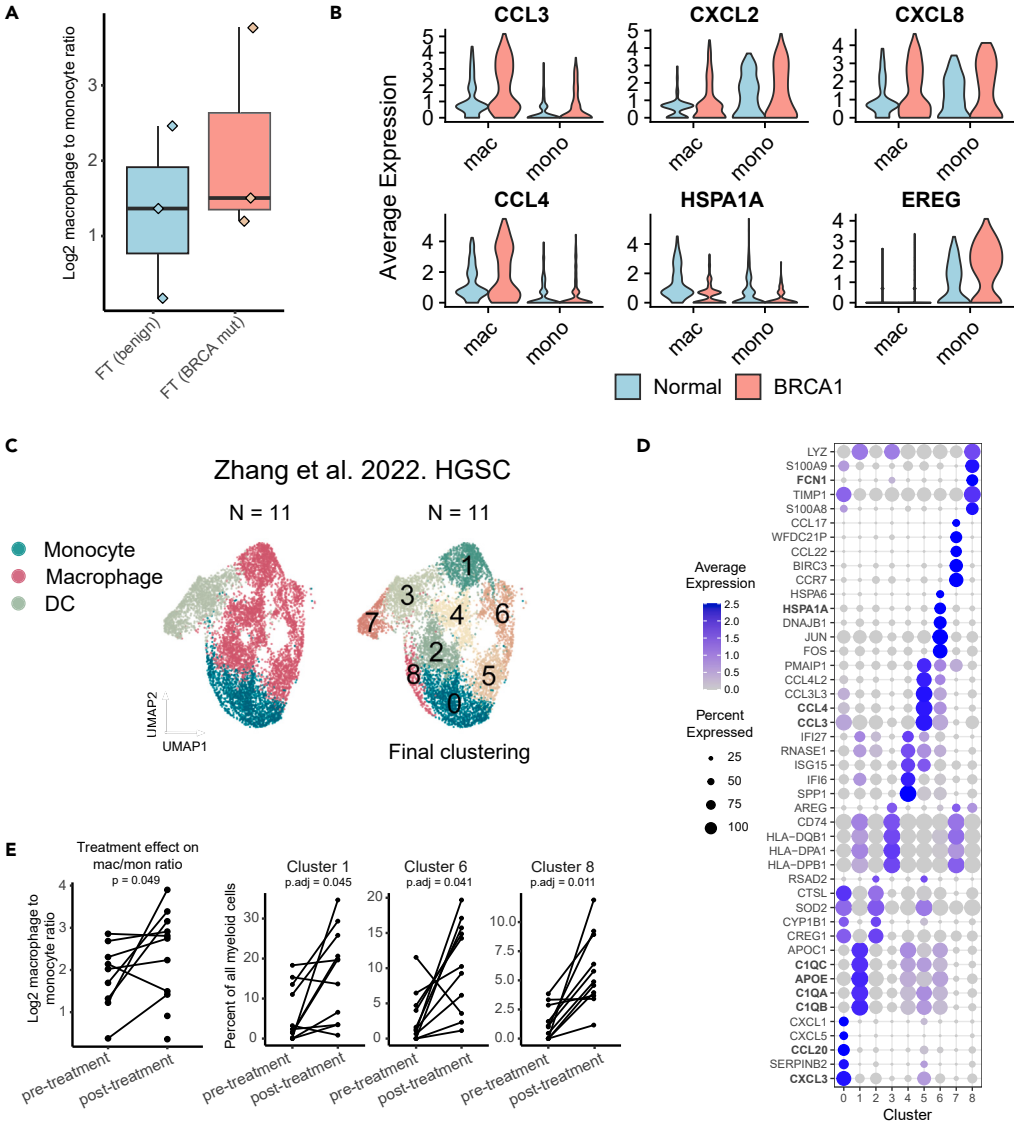

Figure 5. Macrophage and monocyte heterogeneity analysis show the altered gene expression in high-risk patients with germline BRCA mutations and response to chemotherapy

(A) The log2 macrophage-to-monocyte ratio in benign FT compared with FT in germline *BRCA1* carriers (Yu et al. 2022[25]) (N = 3 patients, each).

(B) Examples of monocytic genes defined in human FTs are differentially expressed in FTs of *BRCA*1 carriers. Values shown are normalized RNA expression.

(C) UMAP and clustering reanalysis of myeloid cell subsets from 11 donors pre- and post-neoadjuvant chemotherapy.[26]

(D) Differential expression analysis, calculated from MAST's generalized linear model of myeloid subsets shows z-scaled expression across clusters.

(E) Evaluation of macrophage-to-monocyte ratios and abundance of myeloid subsets from paired pre-and post-chemotherapy treated samples. Clusters 1 and 6 (macrophages) and cluster 8 (monocytes) were significantly enriched post-treatment (two-sided paired t-test, FDR-adjusted p values <0.05). All comparisons are shown in Figure S5D.

of heterogeneity compared to the previous characterization using flow cytometry[22] and importantly highlights the altered myeloid landscape across HGSC and adjacent normal tissue. An independent, human scRNA-Seq dataset[24] shows the cell types identified here were reproducible. Specifically, we identified 5 fibroblast and smooth muscle cell subsets and 2 pericyte subsets, including a rare subset expressing antigen-presenting markers recently found in several tissues and cancer types. A fibroblast subset expressing *C7* was transcriptionally similar to an inflammatory CAF signature found in scRNA-Seq of HGSCs[19] and was most enriched in mesenchymal subtypes of TCGA compared to our other stromal subsets. CCI analysis predicted stromal cells as having the most frequent interactions in human FT with unique ligand-receptor interactions defined in *C7* fibroblasts. These interactions included fibronectin (*FN1*) which correlates with reactive stroma and recurrence after chemotherapy treatment.[53] The *FN1* interactions (*FN1-CD44*) from fibroblasts to immune cells were also increased in tumors relative to non-malignant tissues.

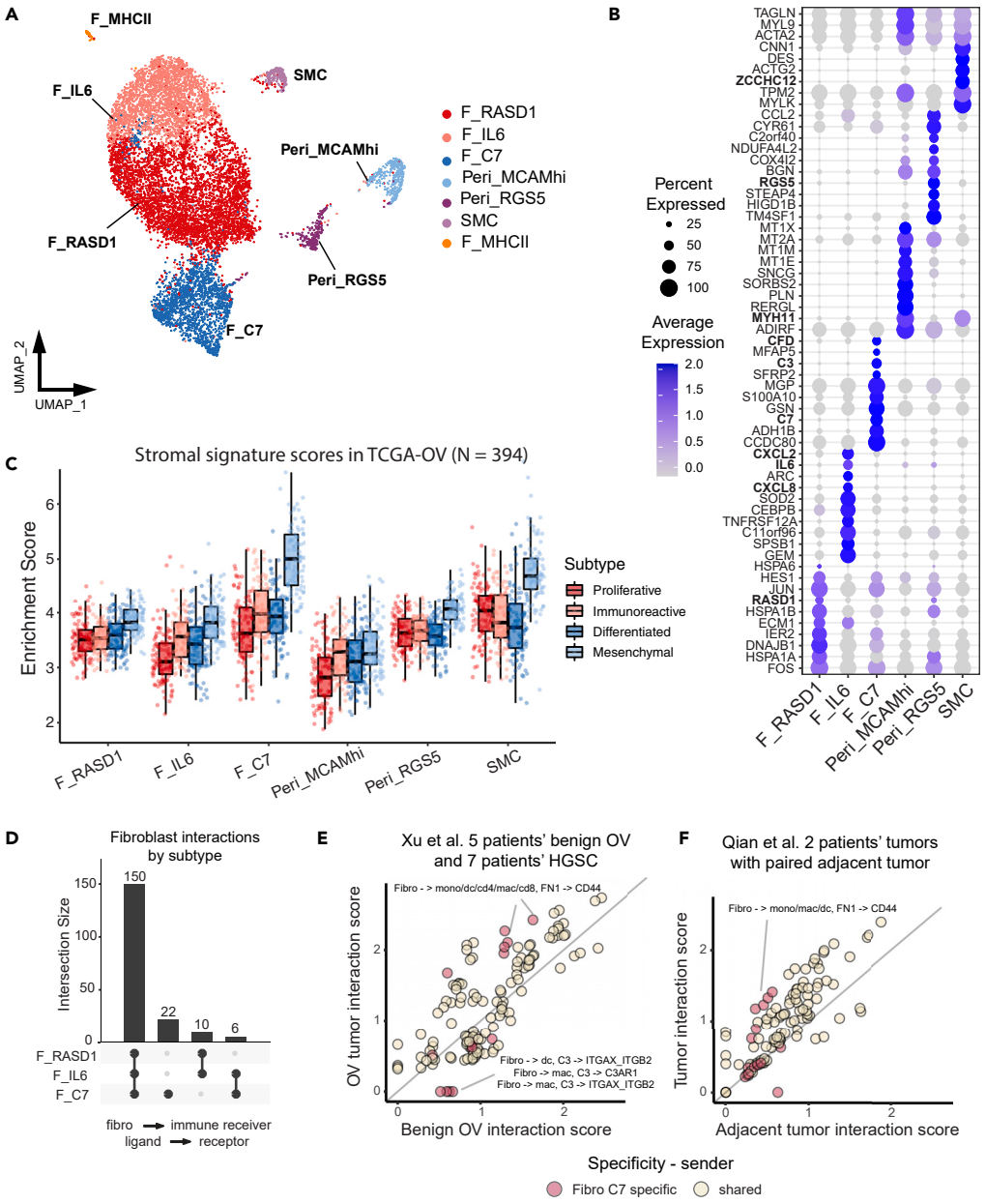

Figure 6. Stromal heterogeneity analysis of human FTs shows the enrichment of complement-expressing fibroblasts and smooth muscle cells in the mesenchymal HGSC subtype

(A) UMAP projection of 4 fibroblast subsets, 1 smooth muscle cell subset, and 2 pericyte subsets from Dinh et al. 2021[13] (n = 11 FT samples, Table S1).

(B) Top 10 DE genes of stromal subsets presented by DotPlot; expression values are z-scaled across clusters. Extended differential expression analysis in Table S2.

(C) Stromal subset signature enrichment analysis on patients with TCGA-OV (N = 394). Pairwise FDR-adjusted p values are shown in Table S3.

(D) Upset plot shows overlapping ligand-receptor interaction numbers from fibroblast subsets to immune cells derived from Cellchat's permutation test.

(E) Stromal CCI co-expression analysis in HGSCs vs. benign ovary.[18] Interactions are represented as sender cell type -> receiver cell type, ligand -> receptor. Fibro: fibroblast, DC: dendritic cell, Mac: macrophage, CD4: $CD4^+$ T cells, CD8: CD8+T cells.

(F) Stromal CCI co-expression analysis in HGSCs vs. tumor adjacent.[14] Interactions are represented as sender cell type -> receiver cell type, ligand -> receptor.

We identified high monocyte diversity in FT with similar gene expression profiles to those observed in circulation (*S100A8/9*, *FCN1*, *VCAN*, and *CD14*).[44,54] Five monocyte subsets were identified along with DCs and macrophages with distinct transcriptional signatures of chemokines, antigen-presentation, transcription factor usage (SCENIC), and pseudotime trajectories. We comprehensively analyzed monocyte heterogeneity at a greater extent than previously in human FT tissues, highlighting the importance of single-cell profiling technology. Compared to benign tissue, we observed a significant increase in the macrophage-to-monocyte ratio in HGSC tumors. Furthermore, monocytes and

macrophages have specific ligand-receptor interactions with other cell types, along with many shared interactions defined by scRNA-Seq. Monocytes with *EREG* expression were predicted to interact with epithelial expressing *ERBB2/4*, a growth factor that might play a role in tumor progression, and macrophages expressing *PDGF*, associated with aggressive HGSC stroma,[48] which may interact with fibroblasts could indicate a role in cancer-associated fibroblast formation in the tumor microenvironment. Interestingly, monocyte-specific interactions are found more frequently in benign tissues, while sone macrophage-specific were higher in HGSC tumors in recent scRNA-Seq data of 12 patients.[18] However, most ligand-receptor pairs defined in monocyte and macrophage interactions were positively correlated in benign and tumor tissues and another scRNA-Seq dataset of 2 patients with matched tissues.[14] Further work is needed to evaluate the mechanisms of monocytic maturation and recruitment in HGSC progression. We suspect that early changes in tumor development may differentiate monocytes in a tissue-specific manner. Others have shown that the co-culture of peripheral blood mononuclear cells (PBMC) derived monocytes with ovarian cancer cell lines was sufficient for alternative macrophage development through TGF-alpha.[55] We hypothesize that the macrophage-to-monocyte ratio could be an indicator of HGSC progression. This concept was recently applied within a melanoma and renal cell carcinoma context,[34] showing that the macrophage-to-monocyte ratio positively correlated with tumor Treg infiltration. Recently published scRNA-Seq of HGSCs also showed a correlation between *FCN1* expressing monocytes and "immunological desert" phenotypes compared to HGSCs with T cell infiltrated or excluded tumors.[19]

Lastly, we evaluated monocyte and macrophage heterogeneity in two publicly available datasets: scRNA-Seq of 3 women with germline BRCA1 mutations with 3 age-matched samples[25] and 11 patients with HGSC with pre and post-neoadjuvant samples.[26] We observed the trend of macrophage-to-monocyte ratio in BRCA1 samples, but the low sample size (N = 3 per condition) limited this analysis. However, we found that BRCA1 samples had higher pro-inflammatory markers, including chemokine expression in their monocytes (*CCL3/4*, *CXCL2/8*) and *EREG* signaling, also found in our CCI analysis. Similarly, only when excluding low abundant samples in the chemotherapy response data,[26] we observed a statistically significant change in the macrophage-to-monocyte ratio between pre- and post-treatment samples, with 2 macrophage and 1 classical $CD14^{+}$ monocyte subsets that were increased after treatment. This data indicates the important but less explored roles of monocytes and macrophages in HGSC progression and response to treatment.

With poor survival outcomes and a lack of early markers for detection, we consider the possibility of immune or stromal signatures as candidates for early disease progression. This work characterizes the phenotypic changes of non-epithelial cell types in human FT and their impacts on HGSC development that promote further studies that lead to immune-based biomarkers of early cancer. We defined the extent of monocyte diversity in FTs, previously overlooked in tissue, as they're typically considered circulating cell types. Emerging data has supported their correlation with tumor phenotypes and potential functions.[34,54,56] The observed transcriptomic differences of monocytes and macrophages in adjacent and tumor tissue and the change in their proportion support their importance in HGSC development and potentially other tumors. However, data from p53 mouse models showed that HGSC can be recapitulated through ovarian and fallopian tube epithelia,[57] indicating more work will be needed to unravel this potential complex of HGSC tumor cells of origin. In summary, our analysis of the non-epithelial microenvironment of the FT has implications for understanding perturbed cell states during HGSC development that may be useful for identifying novel therapeutic targets or biomarkers.

Limitations of the study

Our work has several limitations. The current study will need to be further investigated using mechanistic models. Future work includes using *in vitro* models to evaluate HGSC tumor development in different macrophage-to-monocyte ratio settings. However, *in vivo* experiments, including injecting the mixture of monocyte and macrophages, are challenging given many macrophages are derived from monocytes. Another future direction is to modulate the cell-type-specific cell-cell interaction signaling; however, one would need to overcome the challenge of targeting ligands and receptors, which were generally lowly expressed at mRNA level, compared to the interactions found in both monocytes and macrophages. The lack of clinical data, such as survival, in-depth mutation profiles, and patient treatment details from publicly available HGSC scRNA-Seq data, limits the correlation analysis of immune and stromal cell diversity inferred from FT scRNA-Seq. The limitation of other data modalities, such as high-dimensional flow cytometry, prevents the current findings from further exploration and validation. Additionally, the ability to power these analyses and independently validate the gene expression profiles of the diverse cell subsets was aided by publicly available data; however, we note some of the limitations of this approach. We analyzed these datasets independently as we expect cell type diversity to be lost through a computational dataset integration (CCA, harmony, or similar). We expect dataset-specific biases to be present and cannot verify how differences in sample preparation may have influenced the recovery of cell type proportions. Additionally, multiple samples were derived from different regions within a single patient but were treated as independent in our framework. In total, we had 58 unique patients and 88 total scRNA-Seq samples. The calculation of cell type ratios will be inherently noisy relative to other cell types (stromal cells, T cells), as myeloid cells were less abundant. Finally, others have also shown a significant correlation of $CD68^{+}$ cells in normal fallopian tube epithelia during the luteal phase,[20] and lack the clinical metadata of our samples to identify and account for this trend. Single-cell multimodal transcriptional and epigenomic profiles, such as combined scRNA-Seq and scATAC-Seq have been recently generated for HGSC,[58] which would further provide evidence of HGSC tissue-of-origins at single-cell level. However, the single-cell multimodal for FTs has not been available yet and will be one of the future avenues to explore.

STAR★METHODS

Detailed methods are provided in the online version of this paper and include the following:

- KEY RESOURCES TABLE

- RESOURCE AVAILABILITY
  - Lead contact
  - Materials availability
  - Data and code availability
- EXPERIMENTAL MODEL AND STUDY PARTICIPANT DETAILS
  - Patient specimens
- METHOD DETAILS
  - Biological sample processing for scRNA-Seq
  - Single-cell capture and sequencing
- QUANTIFICATION AND STATISTICAL ANALYSIS
  - ScRNA-seq pre-processing of HGSC samples
  - Single-cell integration of benign FT samples
  - scRNA-seq clustering and subset annotation
  - Quantifying cellular heterogeneity
  - ScRNA-seq signature analysis in TCGA
  - JASMINE pathway analysis
  - Gene regulatory network analysis (SCENIC)
  - Pseudotime/trajectory inference analysis
  - Cell-cell communication analysis
  - Macrophage-to-monocyte ratio across datasets

SUPPLEMENTAL INFORMATION

Supplemental information can be found online at https://doi.org/10.1016/j.isci.2024.108990.

ACKNOWLEDGMENTS

This project was partially supported by the RIDE scholar award 2021 (H.Q.D). The research in the Dinh lab was supported by startup packages from the Human Cancer Genetics and Precision Medicine cluster, Carbone Cancer Center, University of Wisconsin-Madison School of Medicine and Public Health, Vice Chancellor for Research and Graduate Education, and Center for Human Genomics and Precision Medicine. Research reported in this publication was supported by the National Institute of General Medical Sciences of the National Institutes of Health under Award Number T32GM135119 (J.B). The content is solely the responsibility of the authors and does not necessarily represent the official views of the National Institutes of Health. K.L. received funding support from the NIH (R01CA211574) and DOD (W81XWH-22-1-0143). Tumor tissue specimens were collected by the Women's Cancer Biobank within the Department of Obstetrics and Gynecology at Cedars-Sinai Medical Center.

AUTHOR CONTRIBUTIONS

Conceptualization, J.B. and H.Q.D.; methodology, X.L. and J.B.; software, J.B.; formal analysis, J.B.; investigation, J.B. and H.Q.D.; resources, B.R., S.M., and K.L.; data curation, J.B. and M.H.; writing - original draft, J.B. and H.Q.D.; writing - review and editing, J.B., H.Q.D., and K.L.; visualization, J.B.; supervision, H.Q.D. and K.L.; funding acquisition, H.Q.D. and K.L.

DECLARATION OF INTERESTS

The authors declare no competing interests.

Received: October 2, 2023
Revised: January 10, 2024
Accepted: January 17, 2024
Published: January 23, 2024

REFERENCES

1. Lisio, M.-A., Fu, L., Goyeneche, A., Gao, Z.-H., and Telleria, C. (2019). High-Grade Serous Ovarian Cancer: Basic Sciences, Clinical and Therapeutic Standpoints. Int. J. Mol. Sci. *20*, 952. https://doi.org/10.3390/ijms20040952.
2. Medeiros, F., Muto, M.G., Lee, Y., Elvin, J.A., Callahan, M.J., Feltmate, C., Garber, J.E., Cramer, D.W., and Crum, C.P. (2006). The tubal fimbria is a preferred site for early adenocarcinoma in women with familial ovarian cancer syndrome. Am. J. Surg. Pathol. *30*, 230–236. https://doi.org/10.1097/01.pas.0000180854.28831.77.
3. Carcangiu, M.L., Radice, P., Manoukian, S., Spatti, G., Gobbo, M., Pensotti, V., Crucianelli, R., and Pasini, B. (2004). Atypical epithelial proliferation in fallopian tubes in prophylactic salpingo-oophorectomy specimens from BRCA1 and BRCA2 germline mutation carriers. Int. J. Gynecol. Pathol. *23*, 35–40. https://doi.org/10.1097/01.pgp.0000101082.35393.84.
4. Carlson, J.W., Miron, A., Jarboe, E.A., Parast, M.M., Hirsch, M.S., Lee, Y., Muto, M.G., Kindelberger, D., and Crum, C.P. (2008). Serous tubal intraepithelial carcinoma: its potential role in primary peritoneal serous carcinoma and serous cancer prevention. J. Clin. Oncol. *26*, 4160–4165. https://doi.org/10.1200/JCO.2008.16.4814.
5. Shaw, P.A., Rouzbahman, M., Pizer, E.S., Pintilie, M., and Begley, H. (2009). Candidate

serous cancer precursors in fallopian tube epithelium of BRCA1/2 mutation carriers. Mod. Pathol. *22*, 1133–1138. https://doi.org/10.1038/modpathol.2009.89.

6. Piek, J.M., van Diest, P.J., Zweemer, R.P., Jansen, J.W., Poort-Keesom, R.J., Menko, F.H., Gille, J.J., Jongsma, A.P., Pals, G., Kenemans, P., and Verheijen, R.H. (2001). Dysplastic changes in prophylactically removed Fallopian tubes of women predisposed to developing ovarian cancer. J. Pathol. *195*, 451–456. https://doi.org/10.1002/path.1000.
7. Labidi-Galy, S.I., Papp, E., Hallberg, D., Niknafs, N., Adleff, V., Noe, M., Bhattacharya, R., Novak, M., Jones, S., Phallen, J., et al. (2017). High grade serous ovarian carcinomas originate in the fallopian tube. Nat. Commun. *8*, 1093. https://doi.org/10.1038/s41467-017-00962-1.
8. Ducie, J., Dao, F., Considine, M., Olvera, N., Shaw, P.A., Kurman, R.J., Shih, I.-M., Soslow, R.A., Cope, L., and Levine, D.A. (2017). Molecular analysis of high-grade serous ovarian carcinoma with and without associated serous tubal intra-epithelial carcinoma. Nat. Commun. *8*, 990. https://doi.org/10.1038/s41467-017-01217-9.
9. Eckert, M.A., Pan, S., Hernandez, K.M., Loth, R.M., Andrade, J., Volchenboum, S.L., Faber, P., Montag, A., Lastra, R., Peter, M.E., et al. (2016). Genomics of Ovarian Cancer Progression Reveals Diverse Metastatic Trajectories Including Intraepithelial Metastasis to the Fallopian Tube. Cancer Discov. *6*, 1342–1351. https://doi.org/10.1158/2159-8290.CD-16-0607.
10. Lee, Y., Miron, A., Drapkin, R., Nucci, M.R., Medeiros, F., Saleemuddin, A., Garber, J., Birch, C., Mou, H., Gordon, R.W., et al. (2007). A candidate precursor to serous carcinoma that originates in the distal fallopian tube. J. Pathol. *211*, 26–35. https://doi.org/10.1002/path.2091.
11. Lawrenson, K., Fonseca, M.A.S., Liu, A.Y., Segato Dezem, F., Lee, J.M., Lin, X., Corona, R.I., Abbasi, F., Vavra, K.C., Dinh, H.Q., et al. (2019). A Study of High-Grade Serous Ovarian Cancer Origins Implicates the SOX18 Transcription Factor in Tumor Development. Cell Rep. *29*, 3726–3735.e4. https://doi.org/10.1016/j.celrep.2019.10.122.
12. Hu, Z., Artibani, M., Alsaadi, A., Wietek, N., Morotti, M., Shi, T., Zhong, Z., Santana Gonzalez, L., El-Sahhar, S., Carrami, E.M., et al. (2020). The Repertoire of Serous Ovarian Cancer Non-genetic Heterogeneity Revealed by Single-Cell Sequencing of Normal Fallopian Tube Epithelial Cells. Cancer Cell *37*, 226–242.e7. https://doi.org/10.1016/j.ccell.2020.01.003.
13. Dinh, H.Q., Lin, X., Abbasi, F., Nameki, R., Haro, M., Olingy, C.E., Chang, H., Hernandez, L., Gayther, S.A., Wright, K.N., et al. (2021). Single-cell transcriptomics identifies gene expression networks driving differentiation and tumorigenesis in the human fallopian tube. Cell Rep. *35*, 108978. https://doi.org/10.1016/j.celrep.2021.108978.
14. Qian, J., Olbrecht, S., Boeckx, B., Vos, H., Laoui, D., Etlioglu, E., Wauters, E., Pomella, V., Verbandt, S., Busschaert, P., et al. (2020). A pan-cancer blueprint of the heterogeneous tumor microenvironment revealed by single-cell profiling. Cell Res. *30*, 745–762. https://doi.org/10.1038/s41422-020-0355-0.
15. Binnewies, M., Pollack, J.L., Rudolph, J., Dash, S., Abushawish, M., Lee, T., Jahchan, N.S., Canaday, P., Lu, E., Norng, M., et al. (2021). Targeting TREM2 on tumor-associated macrophages enhances immunotherapy. Cell Rep. *37*, 109844. https://doi.org/10.1016/j.celrep.2021.109844.
16. Olalekan, S., Xie, B., Back, R., Eckart, H., and Basu, A. (2021). Characterizing the tumor microenvironment of metastatic ovarian cancer by single-cell transcriptomics. Cell Rep. *35*, 109165. https://doi.org/10.1016/j.celrep.2021.109165.
17. Olbrecht, S., Busschaert, P., Qian, J., Vanderstichele, A., Loverix, L., Van Gorp, T., Van Nieuwenhuysen, E., Han, S., Van den Broeck, A., Coosemans, A., et al. (2021). High-grade serous tubo-ovarian cancer refined with single-cell RNA sequencing: specific cell subtypes influence survival and determine molecular subtype classification. Genome Med. *13*, 111. https://doi.org/10.1186/s13073-021-00922-x.
18. Xu, J., Fang, Y., Chen, K., Li, S., Tang, S., Ren, Y., Cen, Y., Fei, W., Zhang, B., Shen, Y., and Lu, W. (2022). Single-cell RNA sequencing reveals the tissue architecture in human high-grade serous ovarian cancer. Clin. Cancer Res. *28*, 3590–3602. https://doi.org/10.1158/1078-0432.CCR-22-0296.
19. Hornburg, M., Desbois, M., Lu, S., Guan, Y., Lo, A.A., Kaufman, S., Elrod, A., Lotstein, A., DesRochers, T.M., Munoz-Rodriguez, J.L., et al. (2021). Single-cell dissection of cellular components and interactions shaping the tumor immune phenotypes in ovarian cancer. Cancer Cell *39*, 928–944.e6. https://doi.org/10.1016/j.ccell.2021.04.004.
20. George, S.H.L., Milea, A., and Shaw, P.A. (2012). Proliferation in the normal FTE is a hallmark of the follicular phase, not BRCA mutation status. Clin. Cancer Res. *18*, 6199–6207. https://doi.org/10.1158/1078-0432.CCR-12-2155.
21. Shaw, J.L.V., Fitch, P., Cartwright, J., Entrican, G., Schwarze, J., Critchley, H.O.D., and Horne, A.W. (2011). Lymphoid and myeloid cell populations in the non-pregnant human Fallopian tube and in ectopic pregnancy. J. Reprod. Immunol. *89*, 84–91. https://doi.org/10.1016/j.jri.2011.01.014.
22. Ardighieri, L., Lonardi, S., Moratto, D., Facchetti, F., Shih, I.-M., Vermi, W., and Kurman, R.J. (2014). Characterization of the immune cell repertoire in the normal fallopian tube. Int. J. Gynecol. Pathol. *33*, 581–591. https://doi.org/10.1097/PGP.0000000000000095.
23. Lee, S.K., Kim, C.J., Kim, D.-J., and Kang, J.-H. (2015). Immune cells in the female reproductive tract. Immune Netw. *15*, 16–26. https://doi.org/10.4110/in.2015.15.1.16.
24. Ulrich, N.D., Shen, Y.-C., Ma, Q., Yang, K., Hannum, D.F., Jones, A., Machlin, J., Randolph, J.F., Jr., Smith, Y.R., Schon, S.B., et al. (2022). Cellular heterogeneity of human fallopian tubes in normal and hydrosalpinx disease states identified using scRNA-seq. Dev. Cell *57*, 914–929.e7. https://doi.org/10.1016/j.devcel.2022.02.017.
25. Yu, X., Lin, W., Spirtos, A., Wang, Y., Chen, H., Ye, J., Parker, J., Liu, C.C., Wang, Y., Quinn, G., et al. (2022). Dissection of transcriptome dysregulation and immune characterization in women with germline BRCA1 mutation at single-cell resolution. BMC Med. *20*, 283. https://doi.org/10.1186/s12916-022-02489-9.
26. Zhang, K., Erkan, E.P., Jamalzadeh, S., Dai, J., Andersson, N., Kaipio, K., Lamminen, T., Mansuri, N., Huhtinen, K., Carpén, O., et al. (2022). Longitudinal single-cell RNA-seq analysis reveals stress-promoted chemoresistance in metastatic ovarian cancer. Sci. Adv. *8*, eabm1831. https://doi.org/10.1126/sciadv.abm1831.
27. Stuart, T., Butler, A., Hoffman, P., Hafemeister, C., Papalexi, E., Mauck, W.M., 3rd, Hao, Y., Stoeckius, M., Smibert, P., and Satija, R. (2019). Comprehensive Integration of Single-Cell Data. Cell *177*, 1888–1902.e21. https://doi.org/10.1016/j.cell.2019.05.031.
28. Liu, B., Li, C., Li, Z., Wang, D., Ren, X., and Zhang, Z. (2020). An entropy-based metric for assessing the purity of single cell populations. Nat. Commun. *11*, 3155. https://doi.org/10.1038/s41467-020-16904-3.
29. Elyada, E., Bolisetty, M., Laise, P., Flynn, W.F., Courtois, E.T., Burkhart, R.A., Teinor, J.A., Belleau, P., Biffi, G., Lucito, M.S., et al. (2019). Cross-Species Single-Cell Analysis of Pancreatic Ductal Adenocarcinoma Reveals Antigen-Presenting Cancer-Associated Fibroblasts. Cancer Discov. *9*, 1102–1123. https://doi.org/10.1158/2159-8290.CD-19-0094.
30. Dinh, H.Q., Pan, F., Wang, G., Huang, Q.-F., Olingy, C.E., Wu, Z.-Y., Wang, S.-H., Xu, X., Xu, X.-E., He, J.-Z., et al. (2021). Integrated single-cell transcriptome analysis reveals heterogeneity of esophageal squamous cell carcinoma microenvironment. Nat. Commun. *12*, 7335–7415. https://doi.org/10.1038/s41467-021-27599-5.
31. Noureen, N., Ye, Z., Chen, Y., Wang, X., and Zheng, S. (2022). Signature-scoring methods developed for bulk samples are not adequate for cancer single-cell RNA sequencing data. Elife *11*, e71994. https://doi.org/10.7554/eLife.71994.
32. Aibar, S., González-Blas, C.B., Moerman, T., Huynh-Thu, V.A., Imrichova, H., Hulselmans, G., Rambow, F., Marine, J.-C., Geurts, P., Aerts, J., et al. (2017). SCENIC: single-cell regulatory network inference and clustering. Nat. Methods *14*, 1083–1086. https://doi.org/10.1038/nmeth.4463.
33. Zsiros, E., Duttagupta, P., Dangaj, D., Li, H., Frank, R., Garrabrant, T., Hagemann, I.S., Levine, B.L., June, C.H., Zhang, L., et al. (2015). The Ovarian Cancer Chemokine Landscape Is Conducive to Homing of Vaccine-Primed and CD3/CD28-Costimulated T Cells Prepared for Adoptive Therapy. Clin. Cancer Res. *21*, 2840–2850. https://doi.org/10.1158/1078-0432.CCR-14-2777.
34. Mujal, A.M., Combes, A.J., Rao, A.A., Binnewies, M., Samad, B., Tsui, J., Boissonnas, A., Pollack, J.L., Argüello, R.J., Meng, M.V., et al. (2022). Holistic Characterization of Tumor Monocyte-to-Macrophage Differentiation Integrates Distinct Immune Phenotypes in Kidney Cancer. Cancer Immunol. Res. *10*, 403–419. https://doi.org/10.1158/2326-6066.CIR-21-0588.
35. Van de Sande, B., Flerin, C., Davie, K., De Waegeneer, M., Hulselmans, G., Aibar, S., Seurinck, R., Saelens, W., Cannoodt, R., Rouchon, Q., et al. (2020). A scalable SCENIC workflow for single-cell gene regulatory network analysis. Nat. Protoc. *15*, 2247–2276. https://doi.org/10.1038/s41596-020-0336-2.
36. Aziz, A., Soucie, E., Sarrazin, S., and Sieweke, M.H. (2009). MafB/c-Maf deficiency enables self-renewal of differentiated functional

macrophages. Science *326*, 867–871. https://doi.org/10.1126/science.1176056.
37. Rauschmeier, R., Gustafsson, C., Reinhardt, A., A-Gonzalez, N., Tortola, L., Cansever, D., Subramanian, S., Taneja, R., Rossner, M.J., Sieweke, M.H., et al. (2019). Bhlhe40 and Bhlhe41 transcription factors regulate alveolar macrophage self-renewal and identity. EMBO J. *38*, e101233. https://doi.org/10.15252/embj.2018101233.
38. Appel, S., Bringmann, A., Grünebach, F., Weck, M.M., Bauer, J., and Brossart, P. (2006). Epithelial-specific transcription factor ESE-3 is involved in the development of monocyte-derived DCs. Blood *107*, 3265–3270. https://doi.org/10.1182/blood-2005-06-2480.
39. Villar, J., Cros, A., De Juan, A., Alaoui, L., Bonte, P.-E., Lau, C.M., Tiniakou, I., Reizis, B., and Segura, E. (2023). ETV3 and ETV6 enable monocyte differentiation into dendritic cells by repressing macrophage fate commitment. Nat. Immunol. *24*, 84–95. https://doi.org/10.1038/s41590-022-01374-0.
40. Williams, J.W., Tjota, M.Y., Clay, B.S., Vander Lugt, B., Bandukwala, H.S., Hrusch, C.L., Decker, D.C., Blaine, K.M., Fixsen, B.R., Singh, H., et al. (2013). Transcription factor IRF4 drives dendritic cells to promote Th2 differentiation. Nat. Commun. *4*, 2990. https://doi.org/10.1038/ncomms3990.
41. Angerer, P., Haghverdi, L., Büttner, M., Theis, F.J., Marr, C., and Buettner, F. (2016). destiny: diffusion maps for large-scale single-cell data in R. Bioinformatics *32*, 1241–1243. https://doi.org/10.1093/bioinformatics/btv715.
42. Cao, J., Spielmann, M., Qiu, X., Huang, X., Ibrahim, D.M., Hill, A.J., Zhang, F., Mundlos, S., Christiansen, L., Steemers, F.J., et al. (2019). The single-cell transcriptional landscape of mammalian organogenesis. Nature *566*, 496–502. https://doi.org/10.1038/s41586-019-0969-x.
43. Cancer Genome Atlas Research Network (2011). Integrated genomic analyses of ovarian carcinoma. Nature *474*, 609–615. https://doi.org/10.1038/nature10166.
44. Villani, A.-C., Satija, R., Reynolds, G., Sarkizova, S., Shekhar, K., Fletcher, J., Griesbeck, M., Butler, A., Zheng, S., Lazo, S., et al. (2017). Single-cell RNA-seq reveals new types of human blood dendritic cells, monocytes, and progenitors. Science *356*, eaah4573. https://doi.org/10.1126/science.aah4573.
45. Jin, S., Guerrero-Juarez, C.F., Zhang, L., Chang, I., Ramos, R., Kuan, C.-H., Myung, P., Plikus, M.V., and Nie, Q. (2021). Inference and analysis of cell-cell communication using CellChat. Nat. Commun. *12*, 1088. https://doi.org/10.1038/s41467-021-21246-9.
46. Iizuka, K., Naidenko, O.V., Plougastel, B.F.M., Fremont, D.H., and Yokoyama, W.M. (2003). Genetically linked C-type lectin-related ligands for the NKRP1 family of natural killer cell receptors. Nat. Immunol. *4*, 801–807. https://doi.org/10.1038/ni954.
47. Mathewson, N.D., Ashenberg, O., Tirosh, I., Gritsch, S., Perez, E.M., Marx, S., Jerby-Arnon, L., Chanoch-Myers, R., Hara, T., Richman, A.R., et al. (2021). Inhibitory CD161 receptor identified in glioma-infiltrating T cells by single-cell analysis. Cell *184*, 1281–1298.e26. https://doi.org/10.1016/j.cell.2021.01.022.
48. Li, J., Zhi, X., Sun, Y., Chen, M., and Yao, L. (2022). The PDGF Family Is Associated with Activated Tumor Stroma and Poor Prognosis in Ovarian Cancer. Dis. Markers *2022*, 5940049. https://doi.org/10.1155/2022/5940049.
49. Luo, H., Xu, X., Ye, M., Sheng, B., and Zhu, X. (2018). The prognostic value of HER2 in ovarian cancer: A meta-analysis of observational studies. PLoS One *13*, e0191972. https://doi.org/10.1371/journal.pone.0191972.
50. Jeanne, A., Sarazin, T., Charlé, M., Moali, C., Fichel, C., Boulagnon-Rombi, C., Callewaert, M., Andry, M.-C., Diesis, E., Delolme, F., et al. (2021). Targeting Ovarian Carcinoma with TSP-1:CD47 Antagonist TAX2 Activates Anti-Tumor Immunity. Cancers *13*, 5019. https://doi.org/10.3390/cancers13195019.
51. Yang, J., Antin, P., Berx, G., Blanpain, C., Brabletz, T., Bronner, M., Campbell, K., Cano, A., Casanova, J., Christofori, G., et al. (2020). Guidelines and definitions for research on epithelial-mesenchymal transition. Nat. Rev. Mol. Cell Biol. *21*, 341–352. https://doi.org/10.1038/s41580-020-0237-9.
52. Huang, J., Zhou, L., and Deng, K. (2023). Prognostic marker C3AR1 is associated with ovarian cancer cell proliferation and immunosuppression in the tumor microenvironment. J. Ovarian Res. *16*, 64. https://doi.org/10.1186/s13048-023-01140-2.
53. Ryner, L., Guan, Y., Firestein, R., Xiao, Y., Choi, Y., Rabe, C., Lu, S., Fuentes, E., Huw, L.-Y., Lackner, M.R., et al. (2015). Upregulation of Periostin and Reactive Stroma Is Associated with Primary Chemoresistance and Predicts Clinical Outcomes in Epithelial Ovarian Cancer. Clin. Cancer Res. *21*, 2941–2951. https://doi.org/10.1158/1078-0432.CCR-14-3111.
54. Mulder, K., Patel, A.A., Kong, W.T., Piot, C., Halitzki, E., Dunsmore, G., Khalilnezhad, S., Irac, S.E., Dubuisson, A., Chevrier, M., et al. (2021). Cross-tissue single-cell landscape of human monocytes and macrophages in health and disease. Immunity *54*, 1883–1900.e5. https://doi.org/10.1016/j.immuni.2021.07.007.
55. Fogg, K.C., Miller, A.E., Li, Y., Flanigan, W., Walker, A., O'Shea, A., Kendziorski, C., and Kreeger, P.K. (2020). Ovarian cancer cells direct monocyte differentiation through a non-canonical pathway. BMC Cancer *20*, 1008. https://doi.org/10.1186/s12885-020-07513-w.
56. Cheng, S., Li, Z., Gao, R., Xing, B., Gao, Y., Yang, Y., Qin, S., Zhang, L., Ouyang, H., Du, P., et al. (2021). A pan-cancer single-cell transcriptional atlas of tumor infiltrating myeloid cells. Cell *184*, 792–809.e23. https://doi.org/10.1016/j.cell.2021.01.010.
57. Zhang, S., Dolgalev, I., Zhang, T., Ran, H., Levine, D.A., and Neel, B.G. (2019). Both fallopian tube and ovarian surface epithelium are cells-of-origin for high-grade serous ovarian carcinoma. Nat. Commun. *10*, 5367. https://doi.org/10.1038/s41467-019-13116-2.
58. Regner, M.J., Wisniewska, K., Garcia-Recio, S., Thennavan, A., Mendez-Giraldez, R., Malladi, V.S., Hawkins, G., Parker, J.S., Perou, C.M., Bae-Jump, V.L., and Franco, H.L. (2021). A multi-omic single-cell landscape of human gynecologic malignancies. Mol. Cell *81*, 4924–4941.e10. https://doi.org/10.1016/j.molcel.2021.10.013.
59. McGinnis, C.S., Murrow, L.M., and Gartner, Z.J. (2019). DoubletFinder: Doublet Detection in Single-Cell RNA Sequencing Data Using Artificial Nearest Neighbors. Cell Syst. *8*, 329–337.e4. https://doi.org/10.1016/j.cels.2019.03.003.
60. Finak, G., McDavid, A., Yajima, M., Deng, J., Gersuk, V., Shalek, A.K., Slichter, C.K., Miller, H.W., McElrath, M.J., Prlic, M., et al. (2015). MAST: a flexible statistical framework for assessing transcriptional changes and characterizing heterogeneity in single-cell RNA sequencing data. Genome Biol. *16*, 278. https://doi.org/10.1186/s13059-015-0844-5.
61. Korsunsky, I., Millard, N., Fan, J., Slowikowski, K., Zhang, F., Wei, K., Baglaenko, Y., Brenner, M., Loh, P.-R., and Raychaudhuri, S. (2019). Fast, sensitive and accurate integration of single-cell data with Harmony. Nat. Methods *16*, 1289–1296. https://doi.org/10.1038/s41592-019-0619-0.
62. Hafemeister, C., and Satija, R. (2019). Normalization and variance stabilization of single-cell RNA-seq data using regularized negative binomial regression. Genome Biol. *20*, 296. https://doi.org/10.1186/s13059-019-1874-1.
63. Zappia, L., and Oshlack, A. (2018). Clustering trees: a visualization for evaluating clusterings at multiple resolutions. GigaScience *7*, giy083. https://doi.org/10.1093/gigascience/giy083.
64. Gu, Z., Eils, R., and Schlesner, M. (2016). Complex heatmaps reveal patterns and correlations in multidimensional genomic data. Bioinformatics *32*, 2847–2849. https://doi.org/10.1093/bioinformatics/btw313.

STAR★METHODS

KEY RESOURCES TABLE

REAGENT or RESOURCE	SOURCE	IDENTIFIER
Biological samples		
Human ovarian cancer specimens	Cedar-Sinai Medical Center - Women's Cancer Program, Division of Gynecologic Oncology and Department of Pathology and Laboratory Medicine	GEO: GSE233615
Chemicals, peptides, and recombinant proteins		
1x Collagenase/Hyaluronidase	STEMCELL Technologies	7912
Dnase I	Sigma Aldrich	SKU: 10104159001
Minimal Essential Medium (MEM)	Corning	10-010-CV
Critical commercial assays		
Chromium single cell 3' (v3 Chemistry Dual Index)	10x Genomics	PN-1000092
Dead cell removal kit	Miltenyi Biotec	130-090-101
Deposited data		
Source code	This study	Zenodo: https://doi.org/10.5281/zenodo.7958189
Human ovarian cancer scRNA-Seq	This study	GEO: GSE233615
Human benign fallopian tube scRNA-Seq	Dinh et al.[13]	GEO: GSE151214
Human benign fallopian tube scRNA-Seq	Ulrich et al.[24]	GEO: GSE178101
Human wildtype and BRCA1 benign fallopian tube scRNA-Seq	Yu et al.[25]	Mendeley Data: https://data.mendeley.com/datasets/66fz3h924x/1
Human high-grade serous ovarian cancer scRNA-Seq	Qian et al.[14]	https://lambrechtslab.sites.vib.be/en/pan-cancer-blueprint-tumour-microenvironment-0
Human high-grade serous ovarian cancer scRNA-Seq	Olalaken et al.[16]	GEO: GSE147082
Human high-grade serous ovarian cancer scRNA-Seq	Binnewies et al.[15]	GEO: GSE165404
Human high-grade serous ovarian cancer scRNA-Seq	Zhang et al.[26]	GEO: GSE165897
Human benign ovary and high-grade serous ovarian cancer scRNA-Seq	Xu et al.[18]	GEO: GSE184880
Software and algorithms		
R programming language v4.0.3	R core	https://www.r-project.org/
Python v3.7	Python Software Foundation	https://www.python.org/downloads/
Cellranger v3.1.0	10x genomics	10x genomics; https://www.10xgenomics.com/support/software/cell-ranger/downloads/
R package Seurat v4.1.0	Stuart et al.[27]	https://satijalab.org/seurat/
R package DoubletFinder v2.0	McGinnis et al.[59]	https://github.com/chris-mcginnis-ucsf/DoubletFinder
R package MAST v1.16.0	Finak et al.[60]	https://github.com/RGLab/MAST
R package Harmony v0.1.0	Korsunsky et al.[61]	https://github.com/immunogenomics/harmony

(*Continued on next page*)

Continued

REAGENT or RESOURCE	SOURCE	IDENTIFIER
Python package pySCENIC v0.12.1	Van de Sande et al.[35]	https://github.com/aertslab/pySCENIC
R package SCTransform v0.3.3	Hafemesiter et al.[62]	https://github.com/satijalab/sctransform
R scripts Jasmine	Noureen et al.[31]	https://github.com/NNoureen/JASMINE
R package ROGUE v1.0	Liu et al.[28]	https://github.com/PaulingLiu/ROGUE
R package Destiny v3.4.0	Angerer et al.[41]	https://github.com/theislab/destiny
R package Monocle 3	Cao et al.[42]	https://github.com/cole-trapnell-lab/monocle3
R package CellChat v1.4.0	Jin et al.[45]	https://github.com/sqjin/CellChat

RESOURCE AVAILABILITY

Lead contact

Additional information and requests for resources should be directed to Lead Contact, Huy Dinh. (huy.dinh@wisc.edu).

Materials availability

This study did not generate new unique reagents.

Data and code availability

- Raw FASTQ files and h5 files (count matrices) of in-house scRNA-Seq data have been uploaded to NCBI GEO under the following accession code: GEO: GSE233615.
- All source code and datasets generated in this study has been uploaded to a Zenodo repository. (Zenodo: https://doi.org/10.5281/zenodo.7958189) and will be made publicly available upon publication.
- Any additional information required to reanalyze the data reported in this paper is available from the lead contact upon request.

EXPERIMENTAL MODEL AND STUDY PARTICIPANT DETAILS

Patient specimens

This project was performed with approval of the Institutional Review Board at Cedars-Sinai Medical Center (CSMC). All patients provided informed consent. Fresh ovarian cancer samples were collected from women undergoing surgery at Cedars-Sinai Medical Center. Only females were included given that our own and publicly available samples were acquired from fallopian tube or ovarian tissue. The phenotypic and clinical characteristics of the scRNA-seq cohorts are summarized in Table S1.

Low-grade serous cancers samples from donor 1 (samples corresponding to GEO: GSM7431434, GEO: GSM7431435, GEO: GSM7431436, GEO: GSM7431437) were derived from a 33-year-old non-white, non-Hispanic woman. HGSC samples from donor 2 (samples corresponding to GEO: GSM7431438) were derived from a white, non-Hispanic woman of unknown age. HGSC samples from donor 3 (samples corresponding to GEO: GSM7431439) were derived from a 74-year-old white, non-Hispanic woman. HGSC samples from donor 4 (samples corresponding to GEO: GSM7431440) were derived from a 58-year-old white, non-Hispanic woman. HGSC samples from donor 5 (samples corresponding to GEO: GSM7431441, GEO: GSM7431442) were derived from an 85-year-old white, non-Hispanic woman.

METHOD DETAILS

Biological sample processing for scRNA-Seq

Fresh human primary tissues from high-grade (n = 4 patients, n = 5 samples) or low-grade (n = 1 patients, n = 4 samples) serous ovarian tumor patients (Table S1) were placed in sterile serum-free MEM at 4°C and transferred to a tissue culture laboratory. Tissues were minced into ~1–2 mm pieces before digesting with 1 × Collagenase/Hyaluronidase (STEMCELL Technologies, Catalog #: 07912) and 100 μg/mL DNase I (Sigma Aldrich, SKU: 10104159001) in 7 mL of serum-free MEM. The samples were incubated at 37°C with constant rotation for 90 min. The supernatants were collected and the cell suspensions were spun down at 300 g for 10 min at 4°C. To lyse red blood cells, the cell pellets were resuspended in red blood cell lysis buffer (0.8% NH_4Cl, 0.1% $KHCO_3$, pH7.2) and incubated for 10 min at room temperature. Cell suspensions were spun again at 300 g for 10 min at 4°C and the cell pellets were resuspended in PBS. If >5% dead cells were observed by trypan blue staining, dead cell removal was performed using dead cell removal kit (Miltenyi Biotec, Catalog #: 130-090-101) according to the manufacturer's instructions. Remaining cells were directly used for single cell RNA sequencing (scRNA-Seq) or frozen in 90% fetal bovine serum supplied with 10% dimethyl sulfoxide in a Mr. Frosty freezing container placed at −80°C. Frozen cell vials were transferred to gas phase of liquid nitrogen for long-term storage. Cells were thawed and transferred into a 15 mL conical tube with 7 mL of serum-free medium and then spun down at 300 g for 10 min at 4°C. The cell pellets were resuspended in 100 μL of PBS. Cells were counted using a hemocytometer and the sample volume was adjusted to achieve a cell concentration within 100-2,000/μL.

Single-cell capture and sequencing

Single cells were captured and barcoded using the 10X Chromium platform (10X Genomics). scRNA-seq libraries were prepared following the instructions from the Chromium Single Cell 3' Reagent Kits User Guide (v3). Briefly, Gel Bead-In EMulsions (GEMs) were generated using single-cell preparations. After GEM-RT and cleanup, the complementary DNAs (cDNAs) from barcoded single-cell RNAs were amplified before quantification using Agilent Bioanalyzer High Sensitivity DNA chips. The single-cell 3′ gene expression libraries were constructed and cDNA corresponding to an insertion size of ~ 350-400 bp were selected. Libraries were quantified using Agilent Bioanalyzer High Sensitivity DNA chips and pooled together to get similar numbers of reads from each single cell before sequencing on the NovaSeq S4 (Novogene).

QUANTIFICATION AND STATISTICAL ANALYSIS

ScRNA-seq pre-processing of HGSC samples

We downloaded single-cell RNA-seq data from publicly available sources through the NCBI GEO, Zenodo, or like resources (Table S1). Depending on the origin of the source (either gene count matrix or processed data in the Seurat objects), we reanalyzed publicly available data using count matrices for consistent processing. We performed QC[59] and filtered out the low-quality cells with >15% mitochondrial UMIs or fewer than 800 transcripts. Then, we used the single-cell transform (SCTransform) method[62] for expression normalization and regressed out the percent mitochondrial reads and cell cycle scores. Principal components analysis (PCA) was performed from the "SCT" assay prior to integration analysis to remove unwanted technical variance using the Harmony method[61] with default settings. The corrected PCA (Harmony components) were used to generate UMAP embeddings and clusters.

Single-cell integration of benign FT samples

Non-epithelial compartments (stromal, myeloid, and T/NK cells) were subset from a previously published dataset[13] to generate new Seurat objects. Each cell subset was used further integrated analysis across different donors using default 2000 features Integration anchors were calculated using "SCT" as normalization method. The *k.filter* parameter was manually set for myeloid cells and fibroblasts to maintain more donors but kept to default in T/NK subsets where cells were most abundant. Three samples were excluded for myeloid cell analysis and one sample for stromal cell analysis due to the low number of captured cells. The sample IDs and which were used for sub clustering are presented in Table S1.

To validate the presence of our defined cell subsets, we used Label Transfer from Seurat to identify our annotated cluster in an independent cohort of benign FT samples.[24] The two datasets were normalized using SCT and the top 3000 most variable genes were used for PCA. Predicted annotations using the *FindTransferAnchors* and *TransferData* functions. To quantify the similarity between two datasets, the average expression for the top 3000 variable features were used for pairwise correlation analysis of our clusters with the predicted cluster labels and plotted using the Pheatmap package. Similarly, this method was applied in a pairwise correlation analysis was calculated between FT epithelial subsets from Dinh et al. and benign and HGSC samples from Xu et al. 2022.[18]

scRNA-seq clustering and subset annotation

We identified cell clusters using Seurat graph-based clustering methods at increasing resolutions from 0.1 to 1 to identify major cell types (T/NK, stromal, B, myeloid cells) within a scRNA-Seq dataset. We used marker genes – *LYZ*, *CD14*, *CD68*, *FCN1*, *CLEC10A*, *CD1C*, *C1QA/B/C* – to identify myeloid cells, as used in our and other's previous work[13,15,34] were subset and converted into a new Seurat object for further clustering. We re-performed normalization and integration as described on the subset data to identify macrophages and monocytes. Macrophages were characterized by *C1QA*/B/C, *TREM2*, *APOE*, and *HLA-DRA* high expression and monocytes by *FCN1*, *S100A8/9*, and *FCGR3A* for non-classical monocytes. We required a cluster with a minimum of 5% percent of cells from the total cell population. We use the Clustree package[63] to visualize and guide splitting or merging clusters with the following criteria: a minimum of 5 differentially expressed genes using MAST,[60] with a Bonferroni-corrected p-value < 0.01, log2FC > 0.25, and a percent expression difference greater than 25% from the new cluster and its parent in previous clustering resolutions. If these criteria were not met at a clustering resolution, we would merge the cluster back into its parent population and leave the remaining clusters unchanged.

Quantifying cellular heterogeneity

We used the *Rogue* method[28] to quantify the proportion of genes with significant entropy from all expressed genes in a scRNA-Seq sample. We used the RNA counts for myeloid and T/NK cell subsets for entropy scoring and performed initial filtering to require a minimum of 10 cells expressing a gene to be considered for the entropy scoring. Entropy for all donors per cell cluster were calculated using the *SE_fun* function. Rogue scores represent the number of genes determined to have a significant entropy divided by the total number of genes expressed and ranges from 0 to 1. Rogue values were not estimated for samples with fewer than 10 cells per cluster.

In addition, we used DE analysis (adjusted p-value < 0.01, gene expressed in >20% of cells) for all resolutions from 0.1 to 1 using *FindAllMarkers* function in Seurat package. At that given clustering resolution, we sum the unique DE genes of the given subset (myeloid, T/NK, or stromal cells) while excluding mitochondrial and ribosomal genes (MT-, RPS, RPL), divided by the number of unique clusters at that clustering resolution.

ScRNA-seq signature analysis in TCGA

Using the top 10 DE genes per cluster from scRNA-Seq, we computed the average expression (Log normalized counts of transcript per million expression) in TCGA bulk RNA-Seq samples. Two-sided pairwise Wilcox tests were computed for each cluster across the 4 molecular subtypes, using Benjamini-Hochberg FDR p-value correction for multiple comparisons.

JASMINE pathway analysis

Gene set enrichment analysis was performed using Jasmine's odds ratio test.[31] The input data took in the RNA count matrices and used GO:BP genesets from the Gene Ontology database through *MsigDB* (https://www.gsea-msigdb.org/gsea/msigdb). This method was robust against dropouts relative to other gene set scoring methods. We ranked genesets by significance using general linear models and linear contrasts to identify gene sets that were most significant for a given cluster compared to the mean of other clusters. We selected the top 5 pathways per cluster by highest t-value, then z-scaled Jasmine enrichment scores for heatmap visualization after filtering out non-relevant pathways. Enrichment score comparisons were performed using t-test with FDR p-value correction using the Benjamini-Hochberg method. We ranked the pathways by the absolute change by average Jasmine score.

Gene regulatory network analysis (SCENIC)

We applied SCENIC[32] to infer gene regulatory networks in stromal, T/NK, and myeloid cells in benign FT. We used the human hg38 reference with 10kb upstream and downstream from the transcription start sites to search for DNA motifs. AUC scores, which scores the proportion of significantly upregulated genes (or regulons) from a given set of genes using an area under the recovery curve. These scores were generated for each cell and used to create linear models with linear factors with the Multcomp package (v1.4-16; Hothorn et al., 2008). for hypothesis testing. Linear contrasts were constructed using cluster against the mean of the remaining clusters and selected those with the highest t-values. We selected the top regulons for each cell cluster and extracted the T values, representing the cluster-specific enrichment for each regulon that and plotted using ComplexHeatmap[64] package in R. The AUC scores for selected regulon were z-scaled across cell clusters and overlayed onto the Diffusion map.

Pseudotime/trajectory inference analysis

We used the diffusion map method in the Destiny R package,[41] from log-normalized RNA counts from the top variable genes. Spearman's correlation test identified genes associated with the two diffusion map dimensions representing the potential cellular trajectories. We also used *Monocle3*[42] to infer the pseudotime of single cells to independently support the gene expression patterns observed in diffusion map analysis. Antigen presentation scores were calculated by taking the averaged log expression of all HLA genes, and CD74 expressed in a minimum of 10% of cells from any given myeloid cell cluster. Similarly, cytokine scores were calculated using cytokine genes (CXCL-, CCL-, IL-) expressed in 10% of any myeloid cluster. The scores were then overlaid in the inferred trajectories.

Cell-cell communication analysis

To identify potentially interacting cell types, we applied the CellChat method[45] to predict ligand-receptor interactions with default parameters (FDR adjusted p-value < 0.05). We filtered out interactions with CD4 as receptors (with MHCII) on myeloid cell types. We used the predicted macrophage- and monocyte-specific interactions to quantify how ligand-receptor pairs may be co-expressed in different tissues using a similar scoring scheme using the geometric mean from robust means (½ median + $^1/_4$*(first + third quartiles)) of each ligand and receptor expression for each cell cluster.

Macrophage-to-monocyte ratio across datasets

The macrophage-to-monocyte ratio was calculated by the sum of macrophage clusters divided by monocytes per sample in each dataset. We add 1 as a pseudo-count and log2-transform to prevent negative values. Significance was tested using a two-sided Wilcox rank test and corrected using the Benjamini-Hochberg method. In datasets with paired pre- and post- treatment,[26] we used a two-sided paired t.test.